Reply to reviewer #1: Interactive comment on "Continuous online-monitoring of Ice Nucleating Particles: development of the automated Horizontal Ice Nucleation Chamber (HINC-Auto)" by Cyril Brunner and Zamin A. Kanji.

Reviewer comments are reproduced in **bold** and author responses in normal typeface; extracts from the original manuscript are presented in *red italic*, and from the revised manuscript in *blue italic*.

In this technical manuscript, the authors present a new instrument, HINC-Auto, allowing continuous measurements of INP concentrations at fixed temperature and humidity conditions. This instrument is based on the design of the HINC chamber with modifications brought in order to remove the need of a human operator. It is the first paper to report such instrument capable to measure INP concentration online in an automatic way for period that can extend several months. The scientific approach is well built and does not raise any of my concerns. Furthermore, this manuscript is well written and easy to follow. This manuscript is a very valuable source of technicality for the ice community I am in favor of publication after the authors have answer the few questions and recommendations listed below:

We would like to thank the reviewer for the compliments and valuable comments and address the comments individually below.

Line 18: "The interaction between aerosols and clouds contributes to the global energy budget by directly influencing the radiative forcing of the climate system." should read:
"The interaction between aerosols and clouds contributes to the global energy budget by indirectly influencing the radiative forcing of the climate system."

A critical error, thank you! We agree with the reviewer, and changed the sentence as proposed (see line 18 revised manuscript):

The interaction between aerosols and clouds contributes to the global energy budget by indirectly influencing the radiative forcing of the climate system.

Line 66: Presently, no automated online INP counter is available (Cziczo et al., 2017; Lacher et al., 2017). A novel paper has just been submitted to AMTD, several weeks after the present one, showing another automatic online INP counter (expansion type chamber): https://amt.copernicus.org/preprints/amt-2020-307/

We agree with the reviewer, and now include reference to this paper. We correspondingly altered Line 64 (revised manuscript) as stated below. In addition, we learned from the work by Bi et al., 2019, https://doi.org/10.1029/2019JD030609, in which they presented a continuous online INP counter.

A prime limitation for the absence of long term monitoring data sets was that online real-time measurements of INP concentrations via INP counters required human operators as no autonomous online INP counter were available. Bi et al. (2019) presented the first autonomous online INP counter based on a CFDC. A novel paper by Möhler et al. (2020) introduced the Portable Ice Nucleation Experiment (PINE), an autonomous online INP counter that uses the adiabatic cooling during expansion to activate the INPs at the targeted supersaturation.

Line 92: "The surrounding sheath air is dried and filtered before entering the chamber.
missing "dried"

We agree with the reviewer, and changed line 94 (revised manuscript) as proposed:

The surrounding sheath air is dried and filtered before entering the chamber.

Line 121: "A polyvinylidene fluoride (PVDF) spacer physically and thermally separates the two chamber walls."

We agree with the reviewer, and changed line 123 (revised manuscript) as proposed:

A polyvinylidene fluoride (PVDF) spacer physically and thermally separates the two chamber walls.

Figure 3: Red and Green is a bad color combination as it is the most common form of colorblindness.

We agree with the reviewer, and changed Figure 3 such that color is no longer required to read it:

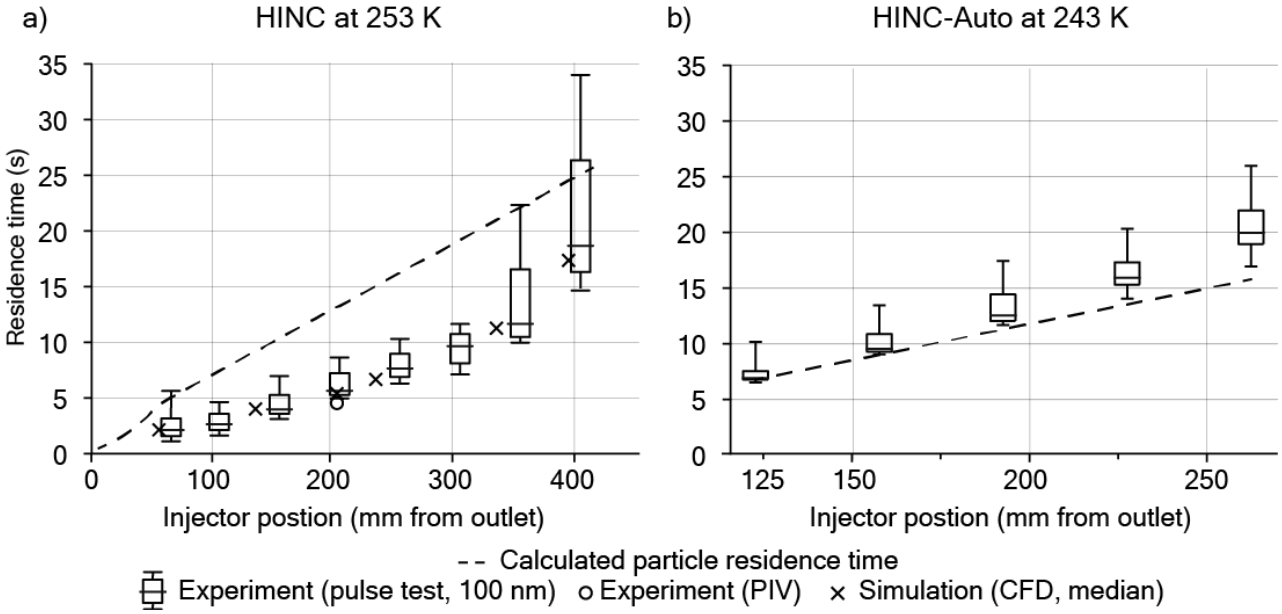

Figure 3.

Figure 3a: How thick is the ice layer and is it included in the calculations (solid line)? The ice layer might decrease the actual volume of the chamber, increase the flow velocity and thus decrease the residence time of particles.

This is a valid statement. The filter paper is 0.5 mm think, if fully soaked with water and frozen 0.6 mm. This translates to a chamber height of 18.8 mm for a freshly replenished ice layers and 19 mm for depleted ice layers. The flow velocity of the center lamina increases by 1.1 % from 19.33 mm/s to 19.54 m/s. We attribute this change to be minor in light of the uncertainty in lamina thickness, S_w and T of the chamber.

Figure 3: It is confusing. If I understood correctly, the message here is that "To smooth the flow field within the chamber and achieve a more consistent desired unidirectional flow field, a mesh was introduced 20 mm downstream of the sheath air injector holes."
For clarity, maybe the legend of Figure 3 could be changed to: "Figure 3. Calculated and measured particle residence time in a) HINC (without mesh) for different injector positions at T = 253 K and b) HINC-Auto (using a mesh to make the flow more laminar) at T= 243 K. Box plots from pulse experiments: median with 25/75% quartiles, whiskers: 5/95% quantiles. Median of PIV experiment (circles, T = 288 K) and CFD simulation (crosses, T = 243 K)." or maybe comparing HINC auto with and without mesh would be more relevant?

We agree with the reviewer, and changed the figure caption of Figure 3 as followed:

Figure 3. Calculated and measured particle residence time in a) HINC (without mesh) for different injector positions at T = 253 K and b) HINC-Auto (using a mesh to achieve a more uniform flow) at T = 243 K. Box plots from pulse experiments: median with 25/75% quartiles, whiskers: 5/95% quantiles. Median of PIV experiment (circles, T = 288 K) and CFD simulation (crosses, T = 243 K).

Figure 4:- "residence time until outlet" is not very intuitive for this figure. I would suggest replacing it by "residence time after entering the chamber" and reverse the time scale. In that way, it is simpler to compare both chamber. The main message here being the effect of cooler temperature entering the chamber, not the total length of the chamber. That way it is easier for the reader to read, that with cooler air, it needs only 20 cm and xx second to reach equilibrium, compare to 30 cm in yy second at warmer sheath air temperature.

Also for a and b legend: I suggest to put temperature first as it is the reason, and length second as it is the consequence. a) T sheath air=298K, (original length, maybe not needed) b)Tsheath air=248 K, (10 cm shorter, maybe not needed)

We agree with the reviewer, and changed the figure legend, time axis scale, and caption of Figure 4 as follows:

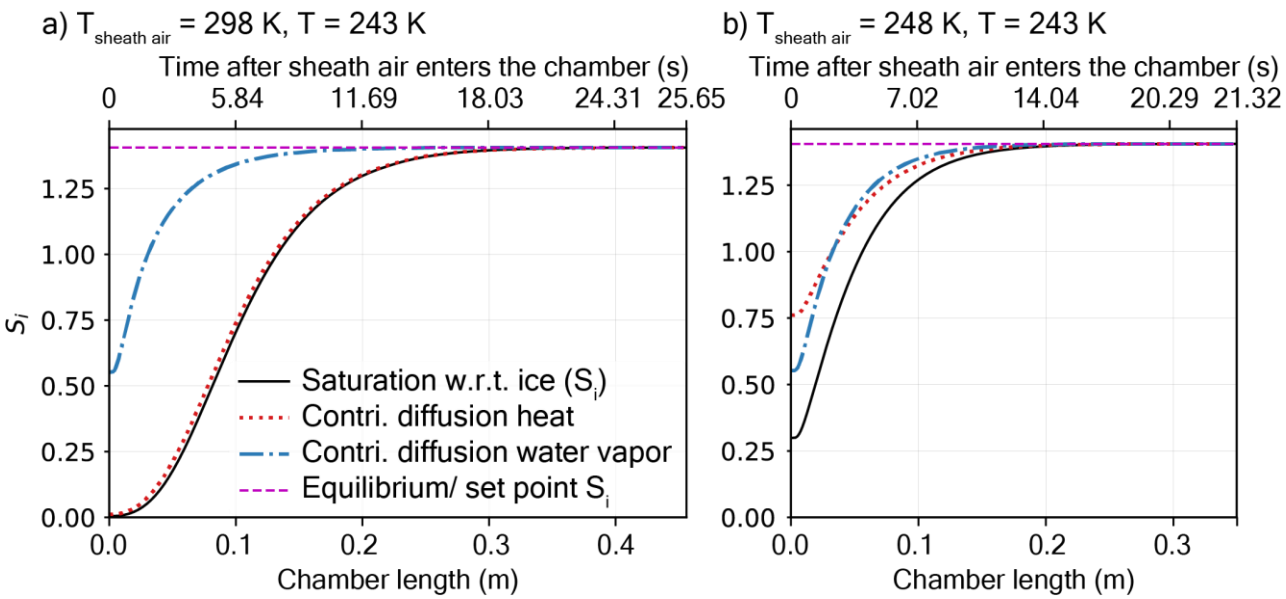

Figure 4. Simulated ice supersaturation development along the chamber's center lamina at T = 243 K and contributing factors diffusion of heat and water vapor for a) $T_{sheath\ air}$ = 298 K (original length) and b) $T_{sheath\ air}$ = 248 K (allowing for the chamber length to be reduced by 10 cm).

Line 210: "The chamber is controlled via a newly developed guided user interface programmed using Python 3.7 and corresponding open source packages. The postprocessing of INP concentrations is done in real time. HINC-Auto can be accessed and controlled remotely if a internet connection is available on site." A suggestion to the authors is to add in the appendix, a screen shot of the software interface could be presented, together with basic parameter that can be set by the user (RH ramping, Temperature profile,. . .).

We agree with the reviewer, and changed the paragraph as follows:

The chamber is controlled via a newly developed guided user interface programmed using Python 3.7 and corresponding open source packages. The postprocessing of INP concentrations is done in real time. HINC-Auto can be accessed and controlled remotely if an internet connection is available on site, however this is

not a requirement for autonomous operation. A screenshot of the guided user interface with comments on the basic parameters a user can set is shown in the appendix (A7-A10).

We further added the following subsection to the appendix:

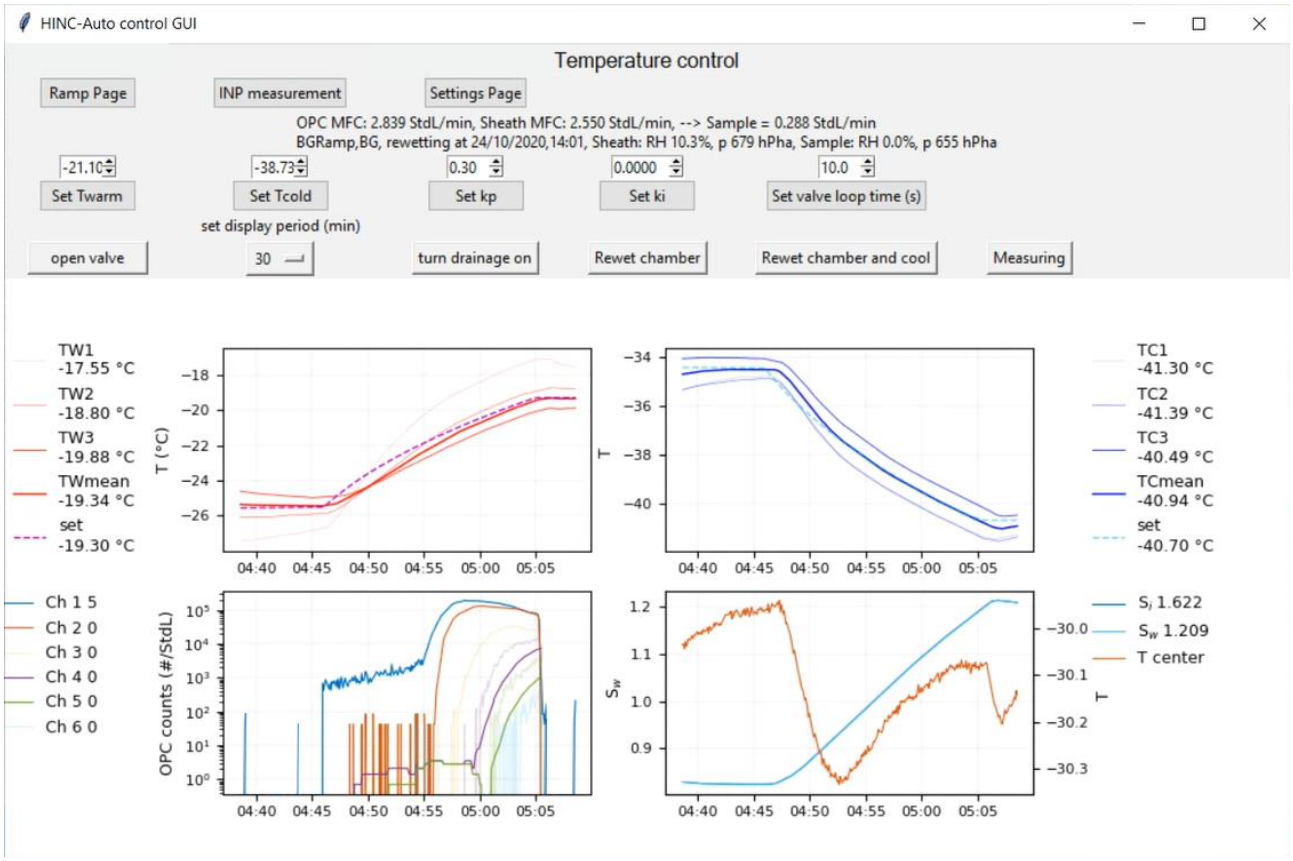

*Figure A8. Main window of the guided user interface used to control HINC-Auto. Top row buttons: **Ramp Page** leads to the window to run S_w- or T-ramps (see Figure A9). **INP measurement** leads to the window to run INP measurements (see Figure A10) and **Settings Page** leads to the window to change additional settings (see Figure A11). **OPC MFC** shows the current flow rate of the OPC mass flow controller (MFC), as reported by the MFC, **Sheath MFC** analogously shows the flow rate of the sheath flow MFC, **Sample** reports the difference between both MFC, which corresponds to the current sample flow rate. **BGRamp** shows the target state of the chamber, in this case "measuring the background after or before a RH- or T-ramp, **BG** shows the state in which the chamber currently is, **rewetting at** indicates the time of the next planned rewetting procedure (UTC), **Sheath** indicates the RH and pressure p of the sheath air as it enters the chamber (measured at mid-height within the chamber upstream of the mesh, thus at the same temperature as the chamber is set to) and **Sample** indicates the RH and pressure p of the sample air (just downstream of the sample diffusion dryer. Center row buttons: **Set Twarm** sets the target temperature of the warm wall, **Set Tcold** sets the target temperature of the cold wall, **Set kp** and **Set ki** set the proportional gain (k_p) and integral gain (k_i) of the PI-controller to control the warm wall temperature, **Set valve loop time (s)** defines the duration of a loop to actuate the warm wall solenoid valve. Bottom row buttons: **open valve** manually opens and closes the warm wall solenoid valve, **Set display period (min)** defines the amount of historic data to be shown in the four graphs below, **turn drainage on** manually actuates the pump to drain the chamber during rewetting, **Rewet chamber** executes the rewetting procedure, **Rewet chamber and cool** executes the rewetting procedure and cools the chamber back down to the set temperature of the chamber before the button was activated, **Measuring** changes the chamber's state and valves to sampling or background measurement. The top left graph shows the warm wall temperature (all three thermocouples, the computed mean wall temperature and the set temperature). The top right graph shows the cold wall temperature (all three thermocouples, the computed mean wall temperature and the set temperature). The bottom left graph shows the counts reported by the OPC for each of the six size-bins/ channels (here CH 1 set to ≥0.3*

µm, CH 2 set to ≥1 µm, CH 3 set to ≥3 µm, CH 4 set to ≥4 µm, CH 5 set to ≥5 µm, CH 6 set to ≥6 µm). The bottom right graph shows S_w and T for the center lamina (calculated).

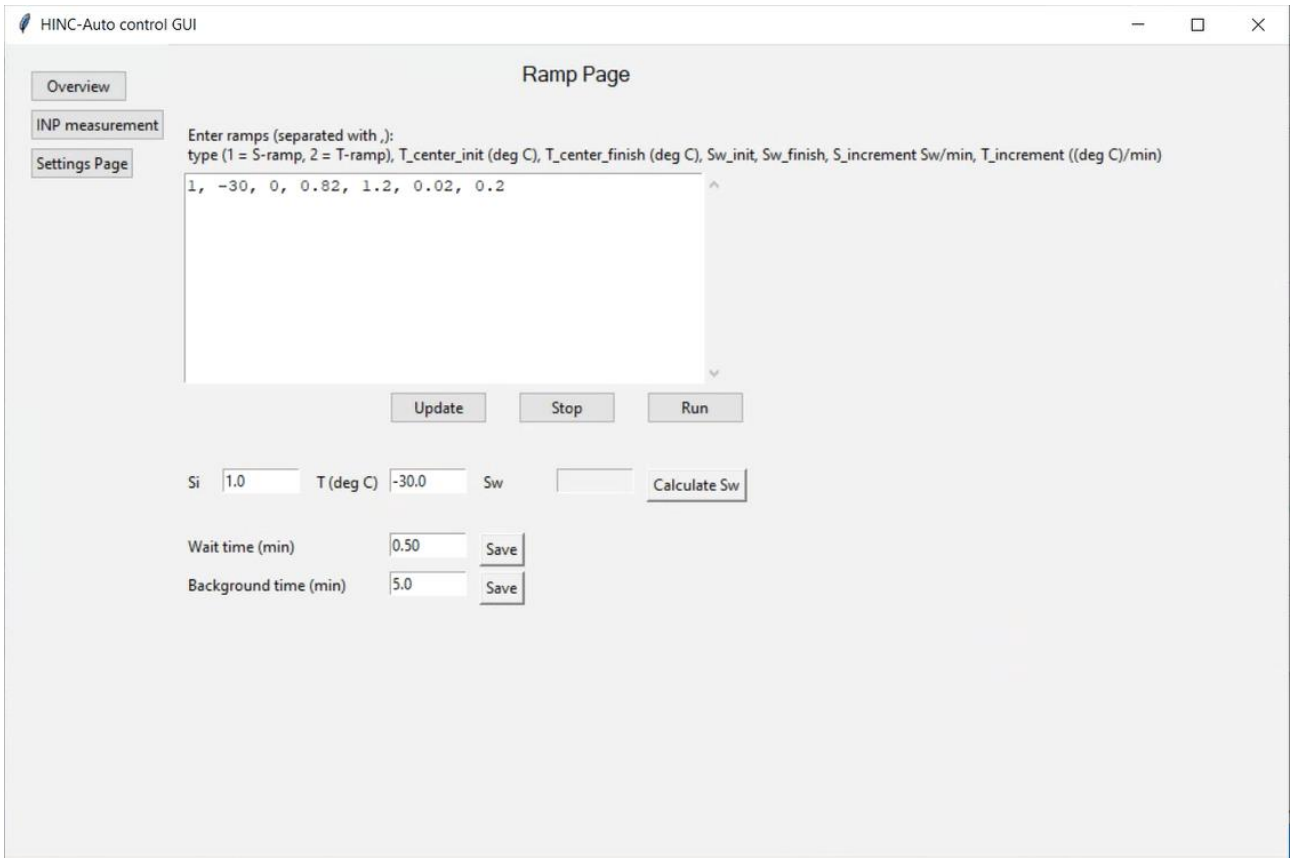

Figure A9. Window of the guided user interface used to control S_w - or T-ramps with HINC-Auto.

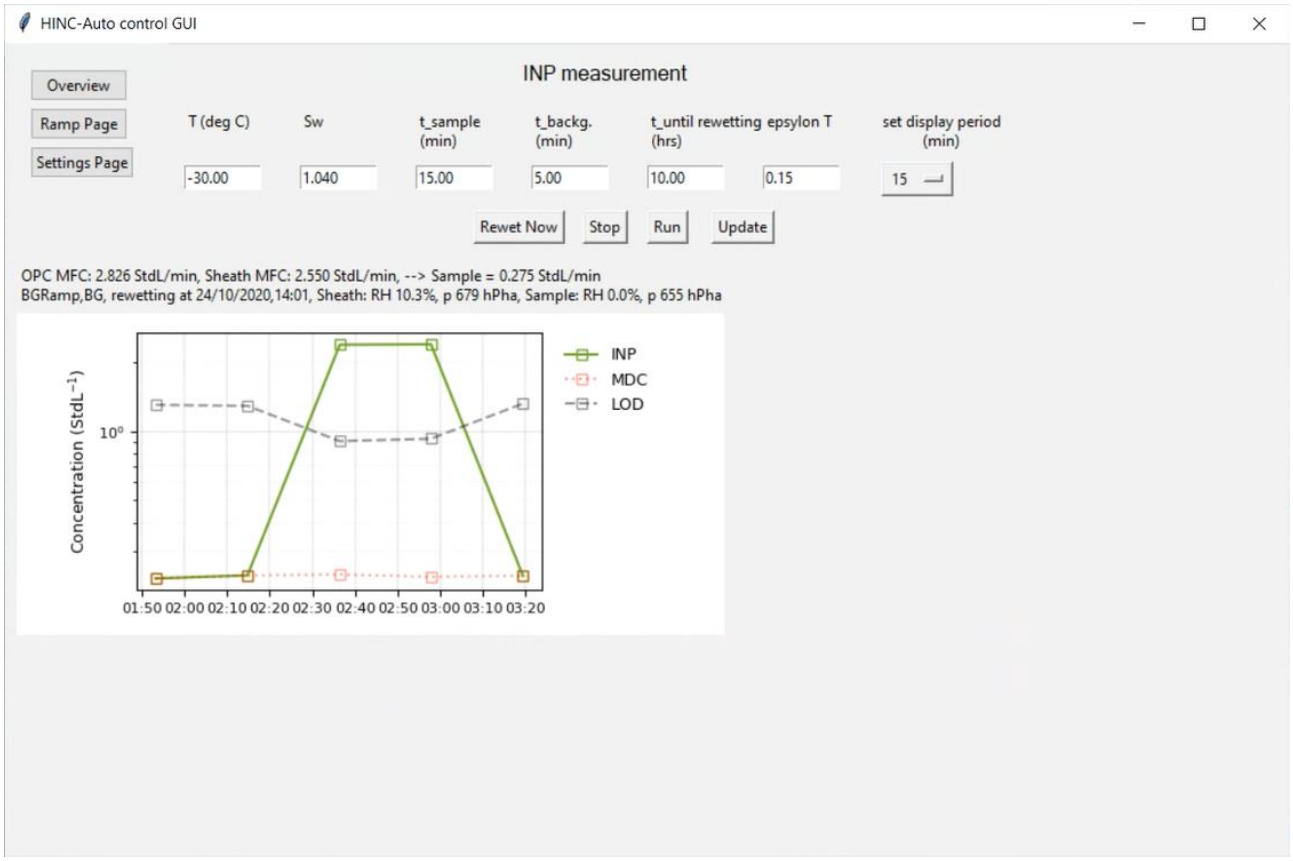

Figure A10. Window of the guided user interface used to control INP measurements with HINC-Auto.

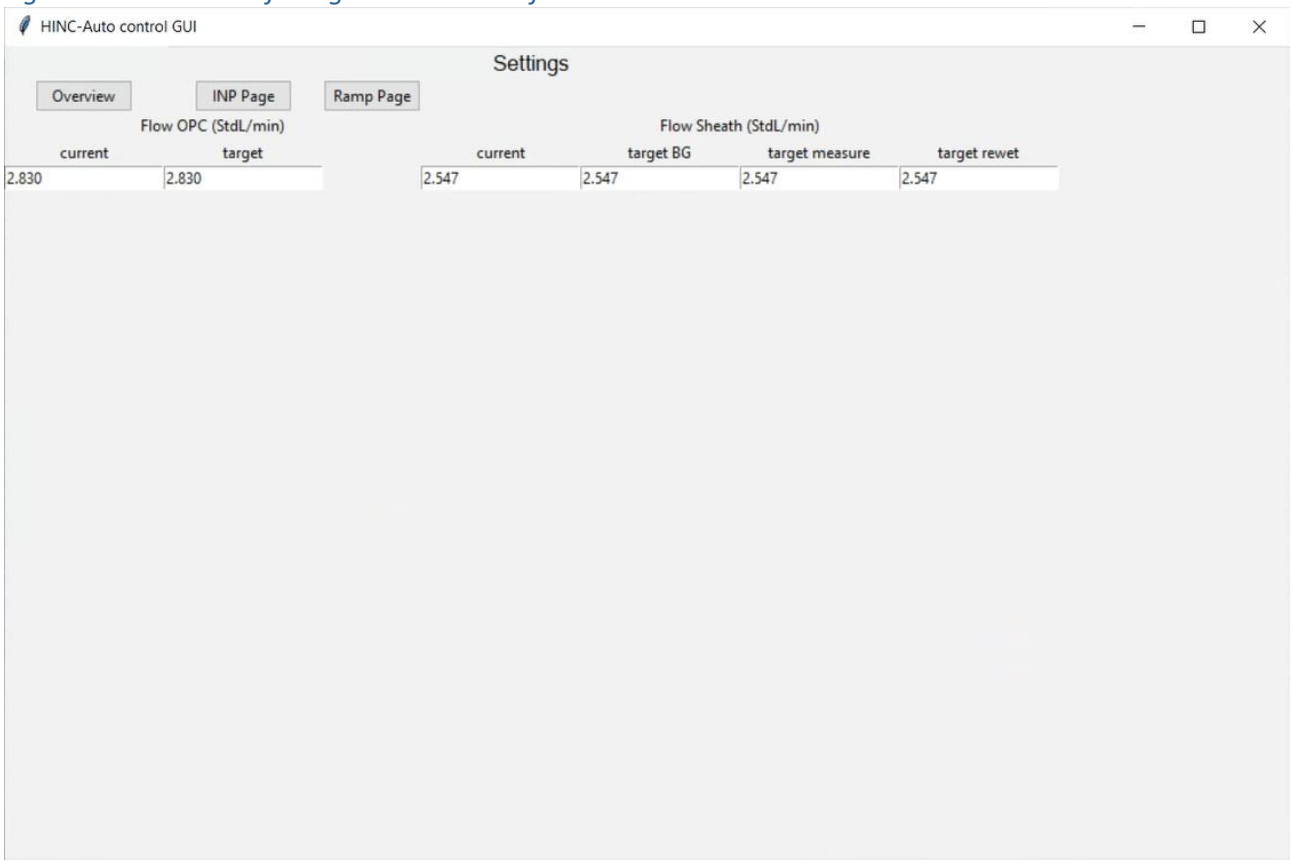

Figure A11. Window of the guided user interface used to adjust additional settings with HINC-Auto.

Line 233: "AF is the ratio of all particles, that are detected in the indicated size bin, to all sampled particles, measured with a CPC within the sample flow." A comment about the smaller particle: The authors discuss about the bigger size of aerosol that can enter HINC auto without being lost due to gravitational loss after activation within HINC-auto. However, what about the other extreme of the particle size distribution, the smaller particle?

We like to thank the reviewer for this important point, since we did not consider commenting on the lower cut-off size of the particles entering the chamber.

What is the (needed) detection limit of the CPC, and why this detection limit was chosen?

The lower the cut-off size is of the CPC the more accurate the ambient aerosol particle counts will be. In the case of the experiments in this work, the CPC has a cut-off size of D50 = 5 nm. This was not actively chosen because for the laboratory measurements we performed experiments with known particles larger tens of nm. The CPC available at the JFJ has a higher size cut-off of D50 = 10 nm. This was also not chosen by us, but it is operated by a different institute under the GAW program.

in other words, is there a minimum size for the particle to enter HINC that could have a chance to activate but not to grow enough to be detected as ice crystal?
For the sampling conditions in HINC (T = 243 K, S_w = 1.04, immersion mode), the smallest particle with the properties of NaCl to be activated would have an initial diameter of 11.4 nm according to Köhler theory. The Kelvin term quickly dominates Köhler theory for these small sizes, thus, a small decrease in initial radius leads to a larger needed increase in activation S_w. Depending on the chemistry of the particle, the initial radius may vary because of the van't Hoff factor or analogous for organic species. If we assume for the solution droplet to immediately freeze after activation it will grow to a diameter of 10.6 µm when having a residence time of 6 seconds in the chamber (diffusional growth by Rogers and Yau (1989)), large enough to be detected by the OPC and differentiated from droplets. We expect that particles with sizes < 12 nm will

therefore not activate into droplets and therefore not freeze, unless they activate by deposition nucleation. Furthermore, we argue that if such particles cannot activate as droplets and freeze by immersion at S_w = 1.04, then they will also not be relevant for ice nucleation in the atmosphere. However, once they coagulate or grow by condensation to sizes larger (> 20 nm) they could activate at lower S_w (< 1.04), which tends closer to atmospherically relevant, at which stage such particles can also activate at our sampling conditions and can be sampled by HINC-Auto. Based on particle loss calculations (von der Weiden et al., 2009) 50% of particles with d = 10 nm and 98% of particles with d = 3 nm are lost in the tubing upstream of the chamber at JFJ.

There is no restriction for small size particle to enter the chamber, would a CPC with very low cutoff size recommended?

A CPC with a very low cutoff point is not necessary in this case because small particles (< 12 nm) would not activate in HINC-Auto, but also not activate in the atmosphere given that S_w > 1.04 would be required as such, these do not need to be counted for estimating atmospherically relevant INP concentrations. Particles smaller than 12 nm resulting from new particle formation (NPF) for example would have to grow by coagulation to become of sizes large enough to activate into droplets and act as INPs in the immersion mode (or in the deposition mode at T < 235 K), however since INP activity scales with surface area, the contributions of particles below 12 nm is not of concern, in fact studies have proposed 100 nm to be the lower size limit for INPs (Pruppacher and Klett, 1997).

Or is there enough small particle loses due to diffusion prior to enter the chamber, in that case what is the cut of size of HINC? or in other word, how can we be sure that all particle that enter HINC and are counted in CPC, can have the possibility to grow big enough to be counted as ice crystal? Can HINC-auto able to measure INP properties of new particle formation that are of size of 5 nm?

In short no, 5 nm particles would need S_w > 1.04 to activate as immersion INPs. So any chamber running at S_w < 1.04 will not be able to account for INPs arising from a 5 nm particle due to Köhler theory limitations, regardless of diffusion losses. However, as we present above, the penetration size of particles into HINC-Auto is 10.3 nm (d_{50}) with 98% of 3 nm particles being lost (particle loss calculator, von der Weiden et al., 2009). Needless to say, all of these scenarios described by the reviewer above would require small particles to grow further to act as INPs even in the atmosphere, as such a 5 nm particle can also not act as an INP in the atmosphere, since it will not activate at atmospherically relevant S_w. So if particles of 5 nm (or less than 12 nm) do not activate in HINC, these will also not activate to droplets and eventually INPs in the atmosphere, unless they grow larger first by coagulation in which case they can be sampled by and activated in HINC-Auto. As such this is not of concern here.

In summary, the losses from diffusion of very small particles entering the tubing are deemed negligible for the measured INP concentration and thus need not be accounted for here. Further, diffusion losses in our laboratory experiments are also considered negligible because we focused on monodisperse particles of 200 nm or polydisperse particles of illite, where particle concentrations below 50 nm are already quite low and not ice-active (Welti et al., 2009) making it a negligible concern for particles below 12 nm.

Fig6a) Why the activated fraction is not 0 at the beginning? is it a real AF or a background of big non activated particle?

We assume the reviewer refers to the high AF in the 0.3 um channel. We believe that the observed ~15% particles above 0.3 µm are due to double (can be up to 25%*) and triple (up to 5.4%*) charged particles when size selecting 200 nm NH_4NO_3 particles (*calculations see Wiedensohler, 1988). A 5-minute background measurement is carried out before and after each ramp, thus at the low and high end of the tested saturation. The background counts are then linearly interpolated between the saturation and subtracted from the counts obtained during the measurement. The non-zero background count can additionally result from large particles that penetrate the DMA due to the transfer function used. In this

particular experiment, we used a lower sheath to sample flow, resulting in a broader transfer function, thus reducing the quality of mono-disperse selection. We now clarify this in the manuscript in line 326.

The sample preparation is as described in section 3.2 for both chambers with a lower DMA sheath flow of 5 L min^{-1} and a higher sample flow of 1.6 L min^{-1} to feed both chambers and the CPC. This resulted in a broader transfer function within the DMA and consequently more larger and multiple charged particles penetrating the size selection. Due to the hygroscopicity of ammonium nitrate, the multiple charged particles are detected in the ≥ 1 µm OPC size bin after hygroscopic growth at S_w < 0.98. In comparison, measurements in section 3.2 and Figure A5 use a narrower DMA transfer function and show a lower activated fraction below S_w < 0.98 than in the experiment with the broader transfer function. The injector position was chosen to result in residence times of τ ≈ 9 seconds.

Fig6a) Why in opc channel >0.3 um there is a small but steady increase of the AF between 0.85 to 0.98 Sw? Is it due to the hygroscopic growth of particle just smaller than 300nm, which with higher humidity grow bigger than 300 nm?

The reviewer's statement is consistent with our understanding of the observed increase in AF. The fraction of size selected particles with a targeted mobility diameter of 200 nm (and double, triple charged particles) that grow because of hygroscopic growth to sizes with an optical diameter of 300 nm or larger increases steadily as the relative humidity is increased from S_w = 0.85 to 0.98.

Line 261: "In either case, the temperature increases in the direction of the air flow, because of the parallel-flow setup of the cooling liquid (see Figure 2b). Therefore, the resulting total temperature variation in the center between the two cooling walls is T ± 0.24 K." I don't understand how the authors get this value of +/-0.24K.

We like to thank the reviewer for pointing out this uncertainty. We aim to clarify by adding figure 7 (revised manuscript):

3.1 Accuracy

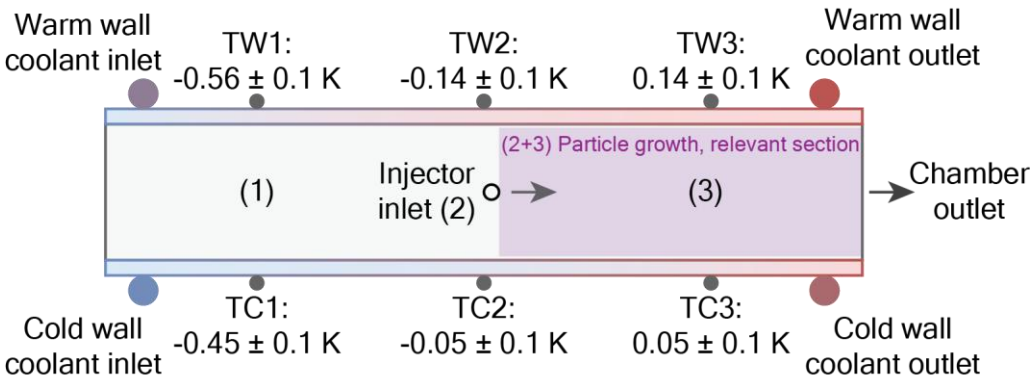

(1): -0.505 ± 0.14 K (2): -0.095 ± 0.14 K (3): 0.095 ± 0.14 K
(2+3): -0.095 - 0.14 to 0.095 + 0.14 K = ±0.24 K

Figure 7. Schematic of uncertainty in temperature measurement showing a side view of HINC-Auto. TW and TC refers to one of six thermocouples installed on the warm wall and cold wall, respectively. Positions (1), (2), (3) and (2+3) indicate the temperature uncertainty of the center lamina. For each of the positions (1), (2), and (3) we have the ± 0.1 K form the warm and ± 0.1 K from the cold wall thermocouple, thus ± $\sqrt{0.1^2 + 0.1^2}$K = ± 0.14.

Four main parameters characterize the INP concentration measured: temperature, supersaturation, particle count and volume flow. The thermocouples have an uncertainty of ± 0.1 K and are calibrated measuring the melting of H_2O and Hg, in close agreement with the ITS-90 (the official protocol of the international

temperature scale). The measured relative (compared to set point T) temperature variation across the warm and cold wall is -0.56/ +0.14 K and -0.45/ +0.05 K at T = 243 K and Sw = 1.04, respectively (see Figure 7). However, on each wall only the two thermocouples close to the injector (TW2/TC2) and the chamber outlet (TW3/TC3) are used to calculate the mean wall temperature. The relative variation therefore decreases to ±0.14 K (at the warm wall) and ±0.05 K (at the cold wall) for a center nominal temperature of T = 243 K at Sw = 1.04. In either case, the temperature increases in the direction of the air flow, because of the parallel-flow setup of the cooling liquid (see Figure 2b). Subsequently, the uncertainty of the center lamina is -0.095 K for the relative variation plus ±0.14 K for the thermocouples uncertainty at location (2) and 0.095 K ± 0.14 K at location (3). Therefore, the resulting total temperature variation in the section relevant for particle nucleation or activation and growth between the two cooling walls is T ±0.24 K. The …

Line 270: "The CPC used for validation experiments has a counting uncertainty of ± 10% which yields in a relative uncertainty in the reported AF of ± 14%" same comment as earlier. how the detection threshold of the CPC affect the AF?

During the validation experiments (subsection 3.2) the sample particles ($(NH_4)_2SO_4$, NaCl, NH_4NO_3) were size selected to a mobility diameter of d_m = 200 nm and in the sedimentation study (Subsection 3.2.2, AgI) to d_m = 100 nm. We believe this should render particles smaller than size cut-off of the CPC used (TSI 3787, D50 = 5 nm) to be negligible contributors to the total particle count. For the INP measurement (Subsection 3.2.3) the NX Illite particles where polydisperse and the SMPS retrieved particle size distribution (Figure 10a) shows more than 4 orders of magnitude lower particle concentrations smaller than 20 nm than between 300 and 500 nm which is substantially below the stated 14% uncertainty in AF. Finally, for the lower size cut-off contribution to field observations please see response to comment about Line 233 above.

Paragraphe 3.2.1: -So here the improvement is due to the flow which is more laminar in HINC-auto, correct? There is no mention of this in the paragraph. -Is this done at particle of size 200 nm? It is not mention in the text.

We agree with the reviewer, and changed the paragraph 3.2.1. as followed:

Figure 8 shows the activation curves of ammonium nitrate size selected to a mobility diameter of d_m = 200 nm and measured at T = 233 K with HINC-Auto compared to measurements performed with HINC. The sample preparation is as described in section 3.2 for both chambers with a lower DMA sheath flow of 5 L min^{-1} and a higher sample flow of 1.6 L min^{-1} to feed both chambers and the CPC. This resulted in a broader transfer function within the DMA and consequently more larger and multiple charged particles penetrating the size selection. Due to the hygroscopicity of ammonium nitrate, the multiple charged particles are detected in the ≥ 1 µm OPC size bin after hygroscopic growth at S_w < 0.98. In comparison, measurements in section 3.2 and Figure A5 use a narrower DMA transfer function and show a lower activated fraction below S_w < 0.98 than in the experiment with the broader transfer function. The injector position was chosen to result in residence times of τ ≈ 9 seconds. The standard sheath to sample flow ratio of HINC-Auto was adjusted to 12:1 to be equal to the ratio used in HINC in order to compare the performance of the two chambers (note that the standard sheath to sample flow ratio of HINC-Auto is 9:1. See section 2.2). HINC-Auto shows an improved precision compared to HINC. We attribute the improvement to the use of the mesh and, subsequently, the more uniform flow within HINC-Auto compared to HINC without the mesh. For measurements in the field with HINC, a defined supersaturation (e.g. S_w = 1.04), temperature and OPC-size bin (e.g. ≥ 4 µm) is used to quantify INPs. Therefore, fluctuations in the activation precision of the ≥ 4 µm size bin can lead to uncertainties in INP concentrations. In the example of HINC, this is equivalent to more than one order of magnitude, thus an improved precision improves the quality of the INP measurements. In addition, particle sedimentation, as expected by theory (see Section below), is visible in the activation curves of HINC-Auto at Sw ≥ 1.02 (see Section 3.2.2).

And if it is monodisperse at 200 nm, why is there an increase of AF bellow 0.975 Sw?

We thank the reviewer for the question. See response to reviewer comment to Fig6a) where we address this concern. Furthermore, we address it in line 326 (revised manuscript).

Line 297: "The sheath to sample flow ratio was 12:1 for both chambers." It was stated Line 267 that the sheath to sample flow ratio should be 9:1. Why is the ratio changed?

The sheath to sample flow ratio of HINC-Auto was adjusted to match the ratio used for the experiments in HINC. This to avoid potential biases when comparing the two chambers (a thinner center lamina results in a steeper activation since the variation in observed temperature and supersaturation is decreased). We added following sentence to Line 297

The standard sheath to sample flow ratio of HINC-Auto was adjusted to 12:1 to be equal to the ratio used in HINC in order to compare the performance of the two chambers (Note that the standard sheath to sample flow ratio of HINC-Auto is 9:1. See section 2.2).

3.2.1 Improvement in precision: Why has –40C been chosen to show the homogeneous freezing onset? At this temperature, the water saturation is very close to the Koop line and it might be hard to distinguish between both. Going lower in temperature would show two distinct activation points.

We agree with the reviewer, for the performance of homogeneous freezing onset, we refer readers to Figure 7 (and Figure A5), where we show experiments below 233 K. The key message of Section 3.2.1 and intended with Figure 8 is to demonstrate the precision increased with HINC-Auto compared to HINC when running multiple experiments.

Line 356: "The for the initial scan (solid line) the sheath flow set to 5 L min−1, and for the second scan to 2 L min−1 (dashed line)." please correct. Also, authors could state that at lower sheath flow, SMPS covers bigger particle size while losing smaller particle size.

We agree with the reviewer, and changed Line 356 as followed:

~~The~~ *For the initial scan (solid line) the sheath flow was set to 5 L min-1, and for the second scan to 2 L min-1 (dashed line). At a lower sheath flow rate, the SMPS scan shifts to cover a larger range of particle sizes while limiting the scanning range at smaller particle sizes.*

Line 359: "This is contradicting our assumption and the lower sheath flow rate of the DMA for the second compared to the first measurement could be the reason." Could it be that with different sheath flow rates, the author can measure at different size range? And also during the time in the stainless steel chamber, coagulation of particle could have made the particles to grow bigger.

We agree with the input of the reviewer about coagulation, and changed Line 359 as followed:

This contradicts our initial assumption of large particles sedimenting more quickly than small particles, thus shifting size distribution towards smaller particle sizes with time. A reason could be due to particle coagulation in the stainless steel aerosol chamber, which causes the observed shift in size distribution towards larger particle sizes.

Line 364: "For atmospheric relevant conditions at the JFJ with 400 cm−3 ≤ N ≤ 1000 cm−3 the drop occurs after 8.5 hours, for 95 cm−3 ≤ N ≤ 200 cm−3 after 13 hours."
- how the authors define the drop? (drop of 20%?) -while the data agree with authors statement (data started at 25/12 and at almost 26/12), later in the experiment, after time 2, the data seems to suggest a need of more frequent rewetting. especially the experiment just after "time 2" and the next one.

The reviewer is correct in asking how we define a drop. Since the drop is gradual, it is not possible to have a stringent cutoff (like 20 or 30%). However, motivated by the reviewer comment we agree that a more

frequent rewetting should be implemented. We now choose to be more conservative and use the drop observed after 8.5 hours as the re-wetting time. As such we now adjust the recommendation to 8 hours for re-wetting and have also adjusted this for the ongoing field measurements (see website). We changed the following sentence Line 369 (initial manuscript) to

Based on the above experiment we choose a rewetting time of 8 hours for field applications in remote areas such as Jungfraujoch.

Line 369: "Based on the above experiment, we chose a rewetting time of 10 hours for field applications (Section 3.3)." As the rewetting is automatic and fast, why not choosing a more frequent rewetting to ensure good data, (i.e. to be on the safe side)?

We agree with the reviewer. We initially choose to do the rewetting sequence less often because of two reasons:

1. The (mechanical/ thermal) stress on the chamber is largest during the rewetting procedure. Frequent rewetting reduces the lifetime of the components and could increase probability of breakdown.
2. If data is acquired over a long period of several months, analysis of the data with subsequent filtering is possible. Because of the large amount of data, ideally will not compromise the quality of the results drastically. The time between two rewetting procedures can then be adapted (which we now do and changed to 8 hours).

Or did the author choose a 10 hours rewetting interval because at higher altitude, residence time is shorter, and in result the water depletion is longer?

No, although we support the reviewer's statement, we did not think of this when choosing the rewetting interval. The rewetting time has now been changed to 8 hours.

Line 378: "Design changes implemented in a second field campaign started in February 2020 resulted in a median LOD of 1.37 std L−1" Could the author specify which design change has been made, which allows a decrease by factor of almost 3 of the LOD? This would be very valuable for the INP community.

We agree with the comment of the reviewer and changed Line 378 as followed:

Design changes implemented in a second field campaign started in February 2020 resulted in a median LOD of 1.37 std L^{-1}. It was observed that ice crystals and frost deposited within the cavity of the chamber outlet. We assumed for supercooled liquid droplets, which make up the majority of the hydrometeor population exiting the chamber, to impact on the surfaces where the Swagelok fitting (to connect the OPC) is inserted into the PVDF frame. The change in inner diameter from the cavity within the PVDF frame (d_i = 10.2 mm) to the fitting (d_i = 3.3 mm) is like a step. The design changes included using a conical drill bit (20°) to smoothen the connection between the chamber outlet and the fitting. In addition, the Swagelok fitting is warmed with a 10 W heat pad during the rewetting procedure to support the evaporation of residual condensate or molten ice that does not drain due to gravity while the chamber is tilted.

Typo: caption fig 8: "with identical particle residence times. of" remove "."

We changed the caption of Figure 8 as proposed by the reviewer. Thanks for catching that.

References

Bi, K., McMeeking, G. R., Ding, D. P., Levin, E. J., DeMott, P. J., Zhao, D. L., Wang, F., Liu, Q., Tian, P., Ma, X. C., Chen, Y. B., Huang, M. Y., Zhang, H. L., Gordon, T. D., and Chen, P.: Measurements of Ice Nucleating Particles

in Beijing, China, Journal of Geophysical Research: Atmospheres, 124, 8065–8075, https://doi.org/https://doi.org/10.1029/2019JD030609, 2019.

Kunert, A. T., Pöhlker, M. L., Tang, K., Krevert, C. S., Wieder, C., Speth, K. R., Hanson, L. E., Morris, C. E., Schmale, D. G., Pöschl, U., and Fröhlich-Nowoisky, J.: Macromolecular fungal ice nuclei in Fusarium: effects of physical and chemical processing, Biogeosciences, 16, 4647–4659, https://doi.org/https://doi.org/10.5194/bg-16-4647-2019, 2019.

Möhler, O., Adams, M., Lacher, L., Vogel, F., Nadolny, J., Ullrich, R., Boffo, C., Pfeuffer, T., Hobl, A., Weiß, M., Vepuri, H., Hiranuma, N., and Murray, B.: The portable ice nucleation experiment PINE: a new online instrument for laboratory studies and automated long-term field observations of ice-nucleating particles, Atmospheric Measurement Techniques Discussions, pp. 1–43, https://doi.org/https://doi.org/10.5194/amt-2020-307, in review, 2020.

Pruppacher, H. and Klett, J.: Microphysics of Clouds and Precipitation, Springer Netherlands, 2 edn., https://doi.org/https://doi.org/10.1007/978-0-306-48100-0, 1997.

Rogers, R. R. and Yau, M. K.: A short course in cloud physics / R. R. Rogers and M. K. Yau, Oxford, Pergamon Press. Rosenfeld, 3, illustrated, reprint edn., 1989.

Von der Weiden, S.-L., Drewnick, F., and Borrmann, S.: Particle Loss Calculator – a new software tool for the assessment of the performance of aerosol inlet systems, 2, 479–494, https://doi.org/https://doi.org/10.5194/amt-2-479-2009, 2009.

Welti, A., Lüönd, F., Stetzer, O., and Lohmann, U.: Influence of particle size on the ice nucleating ability of mineral dusts, Atmospheric Chemistry and Physics, 9, 6705–6715, https://doi.org/10.5194/acp-9-6705-2009, 2009.

Reply to reviewer #2: Interactive comment on "Continuous online-monitoring of Ice Nucleating Particles: development of the automated Horizontal Ice Nucleation Chamber (HINC-Auto)" by Cyril Brunner and Zamin A. Kanji.

Reviewer comments are reproduced in **bold** and author responses in normal typeface; extracts from the original manuscript are presented in *red italic*, and from the revised manuscript in *blue italic*.

In this paper authors described the HINC-Auto, which is automated version of HINC. They describe the technical setup and validation experiments. CFD modeling is also performed. The chamber was deployed in the field and ran for 90 days. The paper is well written, and I recommend publication after following minor points are addressed.

We would like to thank the reviewer for the compliments and valuable comments and address the concerns individually below.

Line 104 -105: Is flow rate affects the buoyancy? Can you have larger gradient but smaller flow rate?

From our understanding, a larger temperature gradient between the warm and cold wall would exacerbate the buoyancy at the warm wall. The difference in buoyancy will introduce shear within the fluid. A smaller flowrate will lead to less shear within the fluid. Thus, increasing the temperature gradient while decreasing the flow rate in order to maintain the same shear is probable. Exactly how the flow rate would influence the buoyancy would require complex 3D fluid dynamics simulations. However, we note that this aspect pertains to vertical chambers, which is not the topic of this paper.

Figure 2: For completeness label the vacuum pump. Currently, the output air is recirculated – closed loop configuration. What is the need of MFC after OPC?

We agree with the reviewer's comment and incorporated the proposition in Figure 2b:

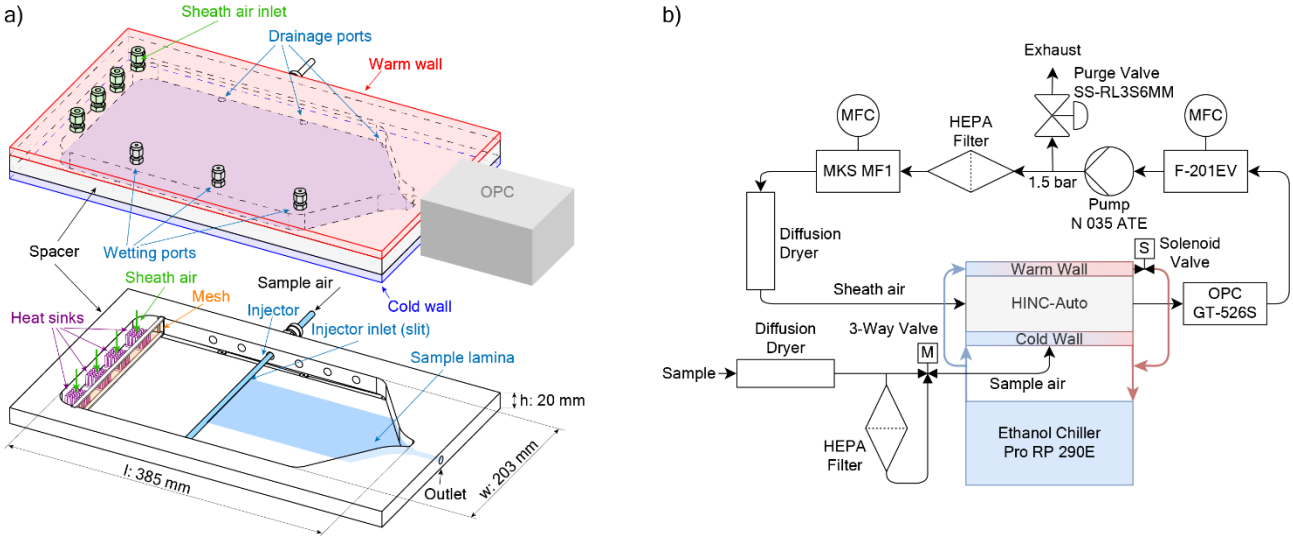

Figure 2.

The MFC after the OPC is needed to maintain a chamber outlet flow rate of 2.83 std L min^{-1}. Controlling both outlet and sheath flow rate allows to indirectly control the sample flow rate without the need of a MCF in the sample flow: chamber outlet flow rate = sheath flow rate + sample flow rate. This is stated in line 147: The sample air flow rate of 0.283 std L min^{-1} results from the difference of the volume flow exiting the chamber through the OPC and the sheath air directed into the chamber.

Line 123: How many layers of filter paper were used.

One layer of filter paper was used. We changed line 124 (revised manuscript) as follows:
The inner metal walls are each covered with one layer of self-adhering borosilicate glass microfibre filter paper (PALL 66217, 1 µm, 8x10") which is wetted with water and acts as reservoir for water vapor in order to create ice and/or water (super)saturation.

Section 2.1: A plot showing the time series of temperature, RH, and droplet diameter would help to understand the operation of the chamber. This plot can include droplet growth, rewetting, and INP measurement periods.

We thank the reviewer for the comment. We already include a time series of RH in Figure 4 and A4 and discuss droplet/ ice crystal growth in section 2.4. Showing one time series with temperature, supersaturation and hydrometeor growth is somewhat arbitrary, as the plot substantially changes for each set temperature, supersaturation, ambient pressure and injector position. Section 2.1 provides just background information over CFDCs without having introduced any concepts like injector position or rewetting/ INP measurement periods. Therefore, we think it is too premature to show Figure 4, A4 or an adaption including hydrometeor growth at this point i.e. in section 2.1.

Line 189: CDF or CFD?

We meant, CFD – thanks for catching that. We changed line 191 (revised manuscript) accordingly:

The 3D CFD simulation revealed for the supersaturation to need a substantial part of the chamber length to equilibrium to the set conditions.

Section 2.4: Regarding particle losses. Is there any size-dependent transmission curve established? Any particular reason why >3 um cannot be transmitted? Because of the presence of any upstream impactor?

We measured the particle counts using an OPC during a Saharan dust event at the JFJ on February 9th, 2020. During the dust event, also particles with an optical diameter of 4.0 µm were present. A 15-minutes cumulative measurement was performed outside next to the total aerosol inlet, at the sample line, where normally the injector of HINC-Auto would be connected (i.e. after the dryer and valve), and at the outlet of the chamber, while both chamber walls were held at 20 °C. Table 1RC2 shows the transmission fraction of the ambient particles. No upstream impactor was used. We believe the horizontally oriented injector tubing upstream of HINC-Auto and injector within HINC-Auto allow for sedimentation, which limits their transmission rate.

	1.0 µm	1.5 µm	2.0 µm	3.0 µm	4.0 µm
Outside, next to Total Inlet	100%	100%	100%	100%	100%
After Dryer + Valve	72%	59%	40%	21%	14%
After Chamber Walls at 20°C	69%	58%	33%	0%	0%

Table 1RC2. Transmission fraction of ambient particles during a Saharan Dust event at the JFJ on February 9th, 2020.

Furthermore, we do not believe this transmission efficiency affects our results in a significant manner since we reach an AF = 0.98 for sampling ambient particles at JFJ (see figure 6, revised manuscript).

How droplet diffusion growth calculations are performed? Can this equation be added to the appendix? It is not clear why d0 = 2 um used. A typical size-distribution at JFJ can be shown to understand what is d0.

We thank the reviewer for highlighting the missing reference. The diffusional growth calculations are according to Rogers and Yau (1989). We added the citation to line 226 (revised manuscript):

Diffusional growth calculations (Rogers and Yau, 1989) … (See continuation of text after the next **reviewer comment**)

Furthermore, we added the following passage to the appendix; line 545 (revised manuscript):

Diffusional growth is calculated according to Rogers and Yau (1989) with the latent heat of sublimation of ice, and latent heat of vaporization of supercooled water according to Murphy and Koop (2005). T and S are variable and feed in from the 2D diffusion model corresponding to the particle's current horizontal and vertical position within the chamber. The diffusional growth of the hydrometeors assumes activation when saturation with respect to ice or water is exceeded.

d_0 = 2µm was used, as it is the largest observed particle diameter able to transmit through the tubing and HINC-Auto at the JFJ. We changed line 221 (revised manuscript) as follows:

The transmission fraction of ambient particles ≥ 2 µm through the tubing and the dry chamber (both walls held at 293 K) on the JFJ is 33%. No ambient particles ≥ 3 µm were transmitted. Therefore, to assess the maximum size of droplets in the following diffusional growth calculations a maximum initial radius of d_0 = 2 µm is used.

How ice crystals are distinguished from water droplets? The description on line 238- 240 is not clear. It is also mentioned that d = 0.2 um grew to 4.57 um. This indicates droplets and ice crystals co -exist. Please clarify.

This is a valid comment, for which we like to thank the reviewer. Stating first the maximum diameters assuming a constant *T* and S_w, then saying, that this is not how particles experience *T* and S_w within the chamber, as *T* and S_w need to equilibrate, and then stating the maximum diameters with variable, equilibrating *T* and S_w is confusing for the reader. Therefore, we altered lines 224-249 (revised manuscript) to explain this more clearly for constant *T* and S_w, and then quantitatively stating the maximum diameters with variable, equilibrating *T* and S_w:

Diffusional growth calculations (Rogers and Yau, 1989) with set fixed T (e.g. constant at 243 K) and S_w (e.g. constant at 1.04) conditions overestimate the final hydrometeor size at the chamber exit since the calculation assumes a constant supersaturation to be maintained for the entire time the particle passes through the chamber. In reality, the saturation in the particle stream needs to equilibrate to the set conditions, thus, the particles are exposed to a lower saturation for the first few seconds (see Figure A4). The 2D diffusion model provides an estimate of the real T and S_w when using the diffusional growth calculations by Rogers and Yau (1989). For an initial diameter of d_0 = 2 µm, liquid droplets are calculated to grow to a maximum size of d_{liq} = 3.31 µm (Zurich, 965 hPa, τ = 9.1 s) and d_{liq} =2.36 µm (JFJ, 645 hPa, τ = 6.1 s). Measurements of a highly hygroscopic aerosol, ammonium nitrate with an initial mobility diameter of d_m = 200 nm (for the sample preparation see Section 3.2) show the onset of cloud droplets (no ice crystals since T > 235 K) in the ≥ 3 µm-size bin at S_w = 1.038, as seen in Figure 6a, and support the calculated maximum size of 3.31 µm at Sw = 1.04. The impact on the final diameter for an initial size of $d_{0\,0.2}$ = 200 nm compared to $d_{0\,2.0}$ = 2 µm is 0.63 µm ($d_{liq\,2.0}$ = 3.31 µm vs. $d_{liq\,0.2}$ = 2.68 µm at 965 hPa and τ = 9.1 s). If the INPs activate as soon as ice saturation is exceeded, the ice crystals grow to $d_{ice\,2.0}$ = 7.77 µm, $d_{ice\,0.2}$ = 7.51 µm at 965 hPa and τ = 9.1 s and $d_{ice\,2.0}$ = 7.66 µm (JFJ, 645 hPa, τ = 6.1 s). Therefore, for experiments performed at T = 243 K and Sw = 1.04, all particles detected in the size bin ≥ 4 µm are considered to be ice crystals formed on INPs. Figure 6b shows a measured activated fraction (AF) curve of ambient air on the JFJ during a high INP concentration period (7:05 22. March 2020, UTC). AF is the ratio of all particles, that are detected in the indicated size bin, to all sampled particles, measured with a CPC within the sample flow. The onset of cloud droplets in the ≥ 0.3 µm size bin exactly at Sw = 1 demonstrates the accuracy of HINC-Auto. At S_w = 1.13 an observed steep increase in AF in the ≥ 3 µm-OPC size bin indicates droplets only grew larger than 3 µm at

this Sw. Compared to the ammonium nitrate measurements performed at Zurich, a delayed activation is observed. This is expected because of the decrease in ambient pressure, which results in shorter residence times, and the much lower hygroscopicity of ambient particles at the JFJ compared to ammonium nitrate. The signal visible in the ≥ 4 µm-OPC size bin comes from INPs, which nucleate and grow to ice crystals at S_w ≥ 1.028 (Si ≥ 1.378). This validates the calculations above that at S_w = 1.04 droplets cannot grow to sizes ≥ 4 µm but ice crystals can, thus supporting the use of the ≥ 4 µm size bin to detect ice crystals.

Equation 1: Define the term [LOD] in the RHS or it is saying the units of LOD are in std Lmin-1 – if so move the units to another line. It is not clear how this equation is formulated. The number '60' in the numerator is confusing. Is this number not used to convert the 'V' into std L per sec from std L per min? If so then units of 'V' should be revised. What are the units of 'BG_counts' parameter?

The RHS term refers to the units of the LOD. We deleted the expression *[LOD] = std L min^{-1}*. Supported by the reviewer comment about **Section 3.3** (see the comment later on) we now show how the INP concentration is calculated. Therefore, some variables (ΣBG counts, $\Sigma N_{BG\ samples}$, V and t_{OPC}) are introduced there and not following the calculation of the LOD in equation (2). We changed line 256 (revised manuscript) as following:

The INP concentration is calculated as follows:

$$INP\ concentration = \left(\frac{\sum INP\ counts}{\sum N_{INP\ samples}} - \frac{\sum BG\ counts}{\sum N_{BG\ samples}}\right)\frac{1}{Vt_{OPC}} \quad (1)$$

where ΣINP counts is the sum of all counts (particle number) in the ≥ 4 µm OPC size bin during the INP measurement, $\Sigma N_{INP\ samples}$ is the total number of OPC intervals during the INP measurement, ΣBG counts is the sum of the background counts (particle number) in the ≥ 4 µm OPC size bin before and after the INP measurement while sampling through a particle filter, $\Sigma N_{BG\ samples}$ is the total number of background OPC intervals before and after the INP measurement, t_{OPC} is the duration of each OPC interval in minutes (here 5 sec, thus 5/60 min), and V is the sample flow rate, here V = 0.283 std L min^{-1}. As the volume flow through the OPC is controlled by the MFC in std L min^{-1}, the resulting INP concentration is INP std L^{-1}.

The limit of detection (LOD) is calculated as follows:

$$LOD = \frac{\sqrt{\sum BG\ counts}}{\sum N_{BG\ samples}}\frac{~~60~~1}{Vt_{OPC}} \qquad ~~[LOD] = \text{std L min}^{-1}~~ \qquad ~~(1)~~\ (2)$$

where the LOD is in std L^{-1}. If over a period of 120 OPC background sampling intervals with a duration of 5 seconds each a total of 3 counts where detected in the ≥ 4 µm OPC size bin, the LOD would be = 0.612 std L min^{-1} ($\Sigma N_{BG\ samples}$ = 120, t_{OPC} = 0.083 min, ΣBG counts = 3, V = 0.283 std L min^{-1}). The stated LOD provides a 62.3% (1 σ) confidence interval.

Concerning the number '60': it was used to convert the OPC duration from seconds to minutes. We changed Equation 1 by removing the '60' and changing the text in line 262 (revised manuscript) from seconds to minutes.

'BG_counts' are just particles where each count represents a particle, so the unit could be particles or number (#). To clarify, we added *"(particle number)"* where we defined background counts in the OPC after equation 1. See line 258 (revised manuscript).

Furthermore, we realized we stated that V is the flow rate through the OPC, which is false. It should be the sample flow rate. We altered the passage in line 262 (revised manuscript) to

…and V is the sample flow rate, here V = 0.283 std L min^{-1}.

Line 250: How many OPC intervals were used, and are they have the same length in terms of time? MDC = 1 count is defined. How this is assumed or calculated?

Each OPC interval is 5 sec in duration (can be set in the OPC). A typical background measurement is 5 minutes, thus 60 intervals. For every INP measurement, there is one background measurement before and after, so 120 intervals in total. The INP measurement is typically 15 min in duration, which is equivalent to 180 intervals.

The minimum detectable concentration is the smallest non-zero signal from the OPC, which is 1 count, divided by the volume of air sampled during the INP measurement, which is 15 min * 0.283 std L min^{-1} = 4.245 std L. Therefore, for the defined INP sampling conditions the MDC is 1/4.245 = 0.2356 INP std L^{-1}. To reduce the level of ambiguity we changed line 270 (revised manuscript) as follows:

The minimum detectable concentration (MDC) is 1 count (particle) in the ≥ 4 µm OPC size bin over a 15-minute INP measurement with a sample flow rate of 0.283 std L min^{-1} ~~over 15 minutes~~, which equals MDC = 0.236 std L^{-1}.

Line 269: clarify '. . .size bin 4995. . .'

According to the manufacturer, the used OPC (MetOne GT-526S) can count 4995 particles per second, and simultaneously classify their optical size and place them in one of 6 user-defined size bins. We changed line 298 (revised manuscript) accordingly:

According to the manufacturer, the used OPC can count 4995 particles per second, and simultaneously classify their optical size and place them in one of 6 user-defined size bins, with an overall accuracy of ± 10% to the calibrated aerosol.

Line 313: Is AF is same FF?

Yes, AF and FF are the same. We changed Figure X (revised manuscript) correspondingly:

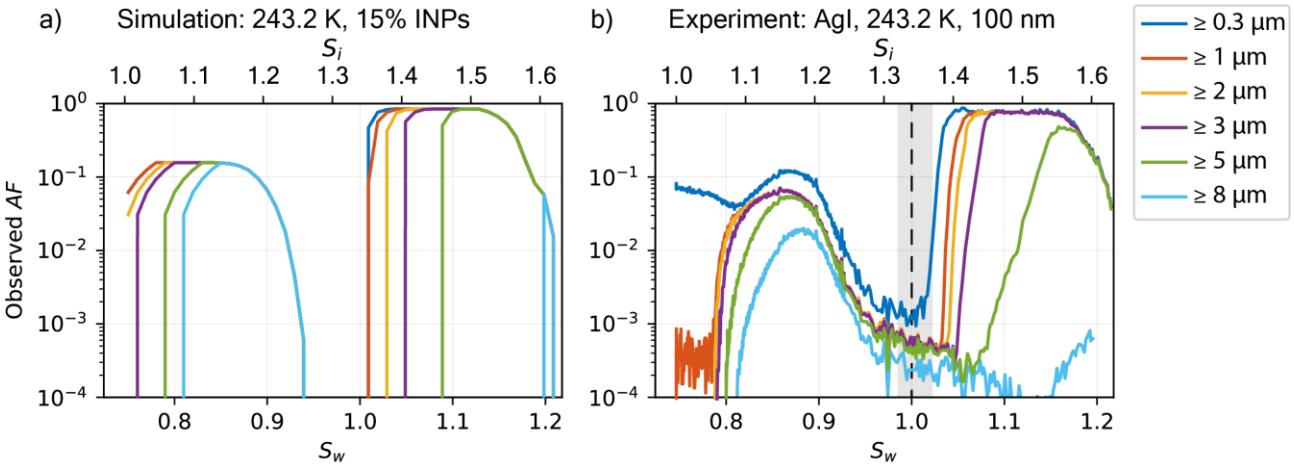

Figure 9. … with a prescribed fraction of INPs of 15% for S_w < 1 and b) … (See continuation of text after the next **reviewer comment**)

Furthermore, we changed line 351 (revised manuscript) correspondingly:

For the simulation, the fraction of INPs has been set to 15% for the simulation to agree best with the experiment. The fraction of INPs depends on the fraction of ice active ϐ-AgI particles within all particles

(Marcolli et al., 2016), which also contain ice inactive α-AgI particles and cannot be deduced by the 2D diffusion model, and therefore, needs to be prescribed.

Figure 9: Add vertical line Sw = 1.04 to panel b to understand AF value. Please comment on AF. Do you achieve maximum droplet activation?

We thank the reviewer for the comment. The aim of Figure 9 is to compare a measurement, where sedimentation of hydrometeors are observed, with the output of the 2D diffusion model. Therefore, we argue a comparison with the supersaturation used for INP measurements (S_w = 1.04) is unrelated to the shown experiment in Figure 9. Instead we add a dotted line to S_w = 1.0 where we also show the chamber uncertainty, and where the AgI particles activate to hydrometeors. We have now clarified the comments of the AF in the figure caption as shown below:

Figure 9. a) Simulated activated fraction curve as a function of S_w with a prescribed fraction of INPs of 15% for S_w < 1 and b) measured activated fraction curve of d_m = 100 nm silver iodide (AgI) particles, both at T = 243 K, with a particle residence time of τ = 13.7 sec at p = 965 hPa. Sizes stated in the legend indicate what fraction of all particles entering the chamber are activated and grow to or beyond the indicated size. Grey shading refers to chamber uncertainty around S_w = 1.0 (see Section 3.1 for details).

We added a sentence discussing whether maximum droplet activation is achieved in line 368 (revised manuscript).

The AF in the experiment as well as in the simulation is leveling off at AF = 0.85 for 1.02 ≤ Sw ≤ 1.13. Ice crystals (≈ 15 % in the experiment) and supercooled droplets are continuously formed at these supersaturations, but ice crystals grow to such large sizes that they sediment and are not detected at the outlet anymore. Therefore, maximum droplet activation of all non-ice active particles is observed in this region. The sedimentation of droplets is observed delayed at Sw ≥ 1.16 compared the model output at Sw ≥ 1.13. This is likely a result of the delayed onset of liquid droplet formation seen in the experiment. While increasing the supersaturation the droplets remain too small, thus their size-dependent settling is delayed, too

Figure 10: The tail end of the size distribution is not shown. It looks significant number of large particles exist. How these large particles (> 1 um) are distinguished from ice crystals?

During the rewetting procedures, when HINC-Auto is held at 25 °C, the chamber is sampling unfiltered air from the sampling line over a period of 2 minutes. During this period, only particles ≤ 2 µm where observed in the corresponding OPC size bins. We therefore distinguish these large particles (> 1 µm) by only using counts in the ≥ 4 µm OPC size to deduce the ice crystal number concentration. As shown in section 3.2.3 if active as CCN these particles are expected to grow to a maximum diameter below 4 µm ($d_{liq\ 2.0}$ = 3.31 at 965 hPa and τ = 9.1 s).

Section 3.3: It is not very clear how AF/FF values are converted to std L min-1 as shown in Figure 11. Please show the equation. Do you use std Temperature and Pressure values?

The AF/FF values are not converted to INP concentration in std L min^{-1}, instead the counts from the OPC are converted to INP concentration. All concentrations are shown in std L^{-1}, as pointed out by the y-axis label. As the flow rate with the mass flow controllers in the HINC-Auto system is set to std L min^{-1}, all concentrations (INP, LOD, MDC) are in std L^{-1} after using this flow rate in the calculations. The MFC measures the pressure and temperature and converts it to standard conditions. As the derivation of the INP concentration is discussed in section 2.4, we added an equation there to line 257 (revised manuscript) to show the derivation of the INP concentration. We moved ΣBG counts, $\Sigma N_{BG\ samples}$, V and t_{OPC} from the after the calculation of the LOD (eq. 2) to this section, as here they are used for the first time.

The INP concentration is calculated as follows:

$$INP\ concentration = \left(\frac{\sum INP\ counts}{\sum N_{INP\ samples}} - \frac{\sum BG\ counts}{\sum N_{BG\ samples}} \right) \frac{1}{Vt_{OPC}} \quad (1)$$

where ΣINP counts is the sum of all counts (particle number) in the ≥ 4 µm OPC size bin during the INP measurement, $\Sigma N_{INP\ samples}$ is the total number of OPC intervals during the INP measurement, ΣBG counts is the sum of the background counts (particle number) in the ≥ 4 µm OPC size bin before and after the INP measurement, $\Sigma N_{BG\ samples}$ is the total number of background OPC intervals before and after the INP measurement, t_{OPC} is the duration of each OPC interval in minutes (here 5 sec, thus 5/60 min), and V is the sample flow rate, here V = 0.283 std L min^{-1}. As the volume flow through the OPC is controlled by the MFC in std L min^{-1}, the resulting INP concentration is INP std L^{-1}.

It is not clear here, but how data is quality controlled? How data is flagged as good or bad. Any outliers are removed? Thoughts on data quality assessment would useful.

This is a very valuable comment, for which we would like to thank the reviewer. We added a corresponding section 2.5, line 272ff (revised manuscript):

2.5 Quality control

The algorithm to derive the INP concentration also performs a quality control. When a deviation from the set conditions (see below) is observed, the data is stored normally but a flag is added to the measurement. The evaluation of the flag and a potential exclusion of the data needs to be done by a researcher during post processing. Deviations are flagged (i) if the mean temperature of either wall is off by more than a predefined value (here ±0.15 K), (ii) one of the two MFCs reports a deviation between the set and the measured flow rate by more than ±50 std mL min^{-1}, (iii) the chiller reports an error, (iv) the pressure within the chamber is different by more than 50 hPa from the ambient pressure or (v) the water reservoir, used to rewet the chamber walls, is below a defined threshold (~100 mL).

References

Murphy, D. M. and Koop, T.: Review of the vapour pressures of ice and supercooled water for atmospheric applications, Quarterly Journal of the Royal Meteorological Society, 131, 1539–1565, https://doi.org/https://doi.org/10.1256/qj.04.94, 2005.

Rogers, R. R. and Yau, M. K.: A short course in cloud physics / R. R. Rogers and M. K. Yau, Oxford, Pergamon Press. Rosenfeld, 3, illustrated, reprint edn., 1989.

Continuous online-monitoring of Ice Nucleating Particles: development of the automated Horizontal Ice Nucleation Chamber (HINC-Auto)

Cyril Brunner[1] and Zamin A. Kanji[1]

[1]Institute for Atmospheric and Climate Science, ETH, Zurich, 8092, Switzerland

Correspondence: C. Brunner (cyril.brunner@env.ethz.ch) and Z.A. Kanji (zamin.kanji@env.ethz.ch)

Abstract. The incomplete understanding of aerosol-cloud interactions introduces large uncertainties when simulating the cloud radiative forcing in climate models. The physical and optical properties of a cloud, as well as the evolution of precipitation, are strong functions of the cloud hydrometeor phase. Aerosol particles support the phase transition of water in the atmosphere from a meta-stable to a thermodynamically preferred, stable phase. In the troposphere, the transition of liquid droplets to ice crystals in clouds, via ice nucleating particles (INPs) which make up only a tiny fraction of all tropospheric aerosol, is of particular relevance. For accurate cloud modeling in climate projections, the parameterization of cloud processes and information such as the concentrations of atmospheric INPs are needed. Presently, ~~no~~ only few continuous real-time INP ~~counter is~~ counters are available and the data acquisition often still requires a human operator. To address this restriction, we developed HINC-Auto, a fully automated online INP counter, by adapting an existing custom-built instrument, the Horizontal Ice Nucleation Chamber. HINC-Auto was able to autonomously sample INPs in the immersion mode at a temperature of 243 K and a water saturation ratio of 1.04 for 97% of the time for 90 consecutive days. Here we present the technical setup used to acquire automation, discuss improvements to the the experimental precision and sampling time, and validate the instrument performance. In the future, the chamber will allow a detailed temporal analysis (including seasonal and annual variability) of ambient INP concentrations observing repeated meteorological phenomena compared to previous episodic events detected during campaigns. In addition, by deploying multiple chambers at different locations, a spatio-temporal variability of INPs at any sampling site used for monitoring INP analysis can be achieved for temperatures $\leq$ 243 K.

1 Introduction

The interaction between aerosols and clouds contributes to the global energy budget by ~~directly~~ indirectly influencing the radiative forcing of the climate system. Yet, predictive climate models struggle to accurately simulate aerosol-cloud interactions, e.g. the Intergovernmental Panel on Climate Change attributed a low confidence level of the aerosol-cloud interactions in their fifth assessment report (Boucher et al., 2013). Clouds containing ice have special relevance to the Earth's climate. Not only does the cloud phase strongly influence climate-relevant physical properties, such as albedo (e.g., Sun and Shine, 1994; Lohmann and Feichter, 2005), but ice is also shown to be responsible for the development of most mid-latitude precipitation processes (e.g., Mülmenstädt et al., 2015). Consequently, it is essential to understand the mechanism of ice formation within mixed-phase

clouds. One such mechanism is immersion freezing, the formation of ice crystals on ice nucleating particles (INPs) immersed in liquid droplets (Vali et al., 2015), which has been studied extensively in laboratory studies (see e.g., Zuberi et al., 2002; DeMott et al., 2003; Marcolli et al., 2007; Lüönd et al., 2010; Niemand et al., 2012; Murray et al., 2012; Atkinson et al., 2013; Hiranuma et al., 2015). A large number of field studies based on intensive observation periods to quantify the concentration, properties, identity and sources of immersion mode INPs have also been reported (see e.g. Dufour, 1862; Rogers and Vali, 1978; Demott et al., 2003; Richardson et al., 2007; Chou et al., 2011; Boose et al., 2016; Lacher et al., 2017). These studies have substantially improved our understanding of such atmospheric INP properties and sources, but some aspects such as diurnal variability, seasonal and and annual trends as well as general spatio-temporal variability of INPs remains poorly constrained (see e.g., Demott et al., 2011; Cziczo et al., 2017; Kanji et al., 2017; Lacher et al., 2018) and insufficiently understood, needing more research to accurately represent atmospheric ice formation in climate models (Demott et al., 2010; Phillips et al., 2013). For example most field studies on INP measurements in the atmosphere have to focus on cases rather than drawing conclusions about the long term trends because of the lack of such data sets. To quantify the free troposphere INP concentration in the Swiss Alps, data from 9 field campaigns over the course of 3 years was required in order to quantify this parameter representing a background INP concentration at a single temperature (242 K) (Lacher et al., 2018), making such research data costly and inaccessible to cloud modellers. Furthermore, with the lack of long term frequent data sets, cloud model research is limited to the small specific case studies for validating INP parameterizations in global or regional climate models (see e.g., Niemand et al., 2012).

To sample INPs, either offline or online techniques are available. In offline INP counters, air is sampled through a filter or an aerosol-to-liquid cyclone impinger. The filter is washed in pure water to extract the sampled aerosols while the cyclone is filled with a small amount of water in which the aerosols accumulate. The sample is then divided into small droplets on cold stages. The freezing of the droplets as a function of temperature allows deducing the INP concentration of the sampled air (Vali, 1971). The advantages of the offline technique are the ability to detect low INP concentrations thus reporting INP concentrations at fairly low (272 K) as well as high supercooling (235 K) (e.g., Conen et al., 2015; Petters and Wright, 2015; Mignani et al., 2019; Wex et al., 2019; Brubaker et al., 2020). Furthermore, the ability of having the aerosols contained for future additional analysis is also possible because not all the sample has to be used in this method of processing and neither is the analysis method of the sample destructive. This comes at the sacrifice of lower time resolution due to the continuous sampling for 8 - 12 hours or more per sample, in order to generate appropriate signal to noise ratio in the freezing spectra. Additional drawbacks include the chance for sample modification when INPs impact the filter or during sample handling and storage (e.g., Cziczo et al., 2017, and references therein). Most recently, Beall et al. (2020) found losses of up to 72% to INP concentration caused by storage at room temperature versus losses of 25% by storage at 253 K over up to 166 days.

Online techniques sample and detect INPs in one step in real time. The measurement of INPs in ambient air is challenging since their number concentrations are on the order of 10^{-1} to 10^{2} std L^{-1} (at 242 K, S_w = 1.04, (see e.g., Lacher et al., 2018; Kanji et al., 2017)) while the sensitivity of portable INP counters is on the order of 10^{-2} std L^{-1} (Cziczo et al., 2017).

This makes online counters good candidates for reporting INP concentrations at moderate (with the presence of aerosol concentrators) to high supercooling ($\leq$ 248 K). Online counters have the advantage of resampling INPs downstream of cloud chambers for further single particle analysis, but often times these measurements are technically challenging and time consuming because of the low concentrations of INPs. Online and offline data acquisition of INP concentrations often needs human operation and is subsequently limited to isolated or planned field campaigns. A ~~handful of ambient INP measurements do exist (Kanji et al., 2017, and references therein). A~~ prime limitation for the absence of long term monitoring data sets ~~is~~ was that online real-time measurements of INP concentrations via INP counters ~~requires human operators . Presently, no automated~~ required human operators as no autonomous online INP counter ~~is available(Cziczo et al., 2017; Lacher et al., 2017) .~~ were available. Bi et al. (2019) presented the first autonomous online INP counter based on a CFDC. A novel paper by Möhler et al. (2020) introduced the Portable Ice Nucleation Experiment (PINE), an autonomous online INP counter that uses the adiabatic cooling during expansion to activate the INPs at the targeted supersaturation. Offline techniques can be automated in their sampling but require substantial sample handling, storage, and finally processing of samples to derive INP concentrations, all by dedicated trained scientists. Furthermore automated aerosol sampling techniques will suffer significantly lower time resolution with the advantage of quantifying INP concentrations at higher temperatures compared to online techniques (Cziczo et al., 2017, and discussion therein).

In this work we present an automated continuous online INP counter, HINC-Auto. Besides a technical description and findings to enhance the chamber precision and sampling time, the chamber is validated with laboratory tests and experiments are compared to a theoretical model. HINC-Auto has been implemented for continuous monitoring of INPs at center temperature (T) = 243 K and and saturation with respect to water (S_w) = 1.04 at the High Altitude Research Station Jungfraujoch (JFJ, 3580 m a.s.l., 46°33' N, 7°59' E). From the collected data set, since Feb 2020, it is expected that a continuous and more detailed temporal analysis of ambient INP concentrations will be possible, thereby observing repeated meteorological episodes compared to previous singular events detected during a single field campaign.

2 Materials and Methods

2.1 Working principle

In the 1980s, continuous flow thermal gradient diffusion chambers were developed to study cloud condensation and ice nucleation (Hussain and Saunders, 1984; Al-Naimi and Saunders, 1985; Tomlinson and Fukuta, 1985; Rogers, 1988). Continuous flow chambers (CFC) used a temperature gradient ∇T to produce water vapor supersaturation in the region between two water- or ice-covered walls. Rogers (1988) defined the term continuous flow thermal gradient diffusion chamber (CFDC) and described the underlying working principle: The annular volume between two vertically oriented concentric cylinders forms the chamber's cavity. The outer and inner walls of the chamber are chilled individually and are covered with a thin layer of ice. For the experiment, one wall is held at a warmer temperature than the other wall, thereby, heat as well as water vapor are diffused from the warm to the cold wall, forming radially linear steady-state temperature and water vapor pressure fields.

Because the saturation vapor pressure with respect to water and ice are exponential functions, a supersaturation with respect to ice, $S_i > 1$, is formed between the two walls. Supersaturation with respect to water $S_w \geq 1$ can be achieved with large enough temperature gradients. A steady flow passes coaxially through the chamber, entraining the sample aerosols in its center lamina. The surrounding sheath air is dried and filtered before entering the chamber. T and S are adjusted to the desired experimental conditions. A more detailed description can be found in Rogers (1988).

The CFDC of Kumar et al. (2003) was developed to probe aerosols and investigate their ability to acts as cloud condensation nuclei (CCN). In contrast to the design of Rogers, the chamber consisted of two horizontally oriented parallel walls. Kanji and Abbatt (2009) altered the design to the University of Toronto CFDC (UT-CFDC) to study ice nucleation at low temperatures. A horizontally oriented ice nucleation chamber offers two major advantages: first, the buoyancy of the air within the chamber resulting from the temperature gradient stabilizes the desired laminar flow. In vertically oriented chambers, the flow is oriented from the top to the bottom. The buoyancy at the warm wall favours an upward vertical air movement which counteracts the overall flow direction. Likewise, the reduced buoyancy at the cold wall adds a relative sinking motion in the proximity of the cold wall. If the temperature gradient is increased such that the shear between the lamina overcomes the fluid's viscous forces, the flow becomes turbulent. The increased mixing not only dislocates the sample particles away from their desired center lamina but also equalizes the temperature and water vapor profiles. The set conditions then may deviate from the assumed values (Rogers, 1988; Stetzer et al., 2008). This happens at gradients larger than 10-15 K, depending on the center lamina temperature (Garimella et al., 2016). Secondly, in horizontally oriented chambers the vapour diffused to the cold wall forming frost tends to stay on the bottom wall because of gravity. In a vertical ice nucleation chamber, the ice grown on the cold wall has the tendency to break off, get carried along with the downward moving sheath flow and is in danger of being misinterpreted as ice formed on an INP. The biggest drawback of the horizontal orientation is the sedimentation of hydrometeors or large aerosol particles. The hydrometeors have to grow to a size of $d \geq 1\,\mu m$ to be detected by the sensor placed at the outlet. For particles $\geq 5\,\mu m$, the terminal sedimentation velocity is such that the hydrometeors are subject to gravitational settling and, depending on their residence time (τ), will not be sampled by the detector.

Lacher et al. (2017) presented the Horizontal Ice Nucleation Chamber (HINC), a close adaption of the UT-CFDC. HINC's record sampling times of 14 h make the chamber's design best suited to be adopted for continuous measurement of ambient INPs. A basic illustration of HINC is shown in Figure 1.

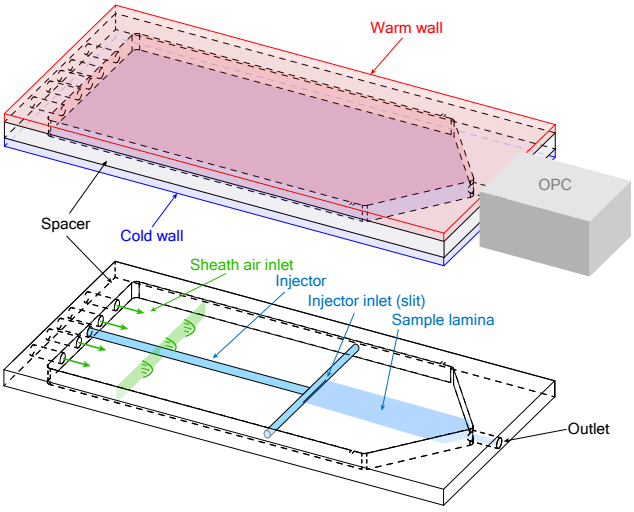

Figure 1. A schematic of HINC, the building platform of HINC-Auto. Top: the entire chamber, bottom: the internal parts.

2.2 HINC-Auto technical setup

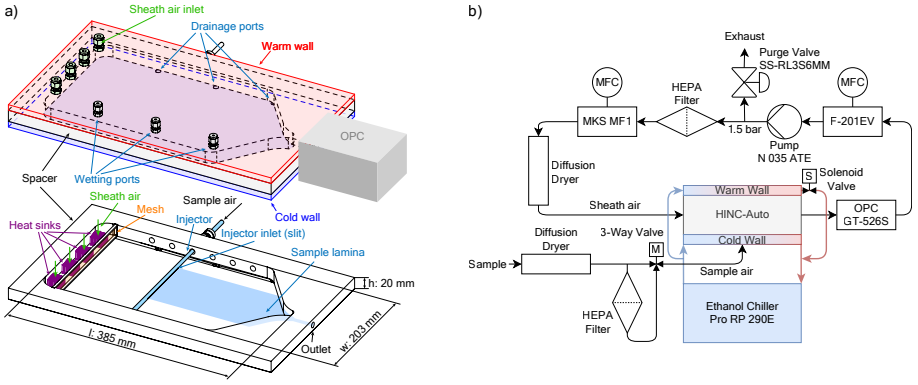

Figure 2. A schematic of HINC-Auto. a) Top: the entire chamber, bottom: the internal parts. b) External components and flow setup.

Figure 2a shows a schematic of HINC-Auto and 2b the external components and flow setup. The chamber consists of two aluminum cooling walls, with a 25 µm copper plating to avoid growth of mold. The chamber walls are cooled with an external recirculating ethanol chiller (Lauda PRO RP 290E), operated in a parallel-flow constellation to the air flow within the chamber.
125 A polyvinylidene fluoride (PVDF) spacer physically and thermally separates the two chamber walls. A cut-out section within the PVDF spacer and the inner surfaces of the metal walls forms the cavity of the chamber. The inner metal walls are ~~covered with~~ each covered with one layer of self-adhering borosilicate glass microfibre filter paper (PALL 66217, 1 µm, 8x10") which is wetted with water and acts as reservoir for water vapor in order to create ice and/or water (super)saturation. During normal operation, the temperature of the bottom wall is equal to or lower than the one of the top wall. The chillers PID-controller

directly controls the bottom wall temperature. A Y-connection just upstream of the bottom wall cooling inlet allows some of the chilled ethanol flow to diverge and flow through the top wall. At the top wall cooling exit, a solenoid valve controls the flow rate of the ethanol through the top wall before feeding it back into the re-circulating bath via the ethanol outlet of the bottom (colder) wall. If the top (warmer) wall is too warm the solenoid is actuated by a PI-controller and if the top wall is too cold, a 12V fan blows room air at the outer surface of the warm wall to increase its temperature. Three thermocouples (Transmetra TEMI313, type K, NiCr-Ni) monitor the temperature on each wall. To expose the aerosol particles within the sample air to a predefined temperature and supersaturation, the sample air has to remain in the center plane between the two chamber walls. Therefore, the center lamina is sandwiched between equal parts of particle-free sheath air. The sheath to sample air ratio is 9 to 1. The mass flow controlled (mass flow controller (MFC) MKS MF1, full scale range: 5 std L min^{-1}, set to 2.547 std L min^{-1}) and dryed (diffusion dryer, $S_\mathrm{w} \leq$0.008 at 20 °C, filled with 4 Å-molecular sieve) sheath air enters the chamber through four holes in the top wall and is blown on to copper heat sinks mounted on the bottom wall. The sheath air is thereby rapidly chilled and flows through a mesh which equilibrates the flow and decreases the degree of turbulence. The weaving plain type 304-stainless steel wire mesh has a mesh-size of 250 mesh inch^{-1} and a wire diameter of 0.04 mm. It spans over the entire width and height of the chamber's cavity (See Fig. 2a). The filter paper coats the cooling walls only downstream of the mesh. A horizontally aligned injector with a outer diameter of 6.35 mm and a slit of 0.4x100 mm^2 is used to guide the sample air into the chamber. The sampled air also passes a diffusion dryer identical to the sheath flow dryer before entering the injector. The injector is mounted through one of six holders in the side wall of the spacer. All unused holes are plugged. Placing the injector in a hole further upstream allows to increase the particle residence time and vice versa. A 6-channel optical particle counter (OPC, MetOne GT-526S) detects the number and size of the particles exiting the chamber via the outlet. A MFC downstream of the OPC (Bronkhorst, F-201EV, full scale range: 3.5 std L min^{-1}) is set to 2.83 std L min^{-1} (defined by the specifications of the OPC). The sample air flow rate of 0.283 std L min^{-1} results from the difference of the volume flow exiting the chamber through the OPC and the sheath air directed into the chamber. Consequently, a well sealed chamber is crucial for a representative operation. Downstream of the OPC and the MFC, a vacuum pump (KNF, N 035 ATE) is used to generate sufficient pressure drop over the MFC and to increase the pressure after the pump. A purge valve (Swagelok, SS-RL3S6MM) purges excess air above the set absolute pressure of 1.5 bar. The air is filtered with a HEPA filter and recycled back into the sheath air MFC.

During operation, water vapor diffuses from the top to the bottom wall, depleting the top wall of the ice layer while adding additional ice to the bottom wall. To maintain the desired supersaturation within the chamber, the top wall ice layer needs to get replenished by re-wetting the filter paper at temperatures $T > 273$ K. This rewetting procedure requires tilting the chamber by 25° using a linear motor to allow excess water and water collected on the cold wall to drain. A peristaltic pump with a flow rate of 10 ml min^{-1} pumps 40 ml water from a water reservoir into one of the three wetting ports, located on the top cooling plate. Two solenoid valves alternate the used wetting port every 10 seconds. During the rewetting procedure a second peristaltic pump with a flow rate of 65 ml min^{-1} is used to drain excess water which is recycled back into the rewetting reservoir. The reservoir is initially filled with 500 ml double-deionized water. The reservoir is protected from day light while a piece of copper

and a UV-LED protects the water from spoilage. The total water uptake of the chamber is 100 ml month^{-1}. The molecular sieves in the diffusion dryers need to be replaced every 30-60 days, depending on the ambient relative humidity. Sensors are used to check both sheath and sample air relative humidity to determine when the molecular sieves require replenishing.

2.3 Design changes

HINC showed differences between the measured and the calculated particle residence times as shown in Figure 3a. The particle residence times were measured with pulse experiments, where a brief pulse of particles ~~is~~ was injected into HINC and then compared to the delayed temporal evolution of the particle counts exiting the chamber. To analyze the discrepancy, a 3D computational fluid dynamics (CFD) simulation was carried out (STAR-CCM+ V13.04.010). The CFD simulation was validated with a particle image velocimetry (PIV) experiment. A detailed description of CFD simulation and the PIV experiment can be found in the appendix (A1). Only after modelling the tubing of the sheath air and corresponding union tee and union cross to distribute the sheath air outside of the chamber, the CFD simulation and the PIV-experiment came into good agreement. The validated simulation showed persistent high velocity regions downstream of the sheath air inlets (see Figure A2) which are not in agreement with the anticipated flow velocities. This explains the lower residence time in pulse tests compared to the calculated residence time, which assumed ideal velocity distributions within HINC. Besides the high velocity jet regions (Figure A2), reversed flows are also present within the chamber, forming two large counter rotating vortices. Particle sedimentation experiments with HINC also confirmed the two vortices. To smooth the flow field within the chamber and achieve a more consistent desired unidirectional flow field, a mesh was introduced 20 mm downstream of the sheath air injector holes. PIV experiments with the mesh installed in HINC showed the anticipated homogenization of the flow velocity. With HINC-Auto pulse tests are now in good agreement with the calculated values as seen in Figure 3b. Therefore, no additional PIV experiments and CFD simulations were performed with HINC-Auto.

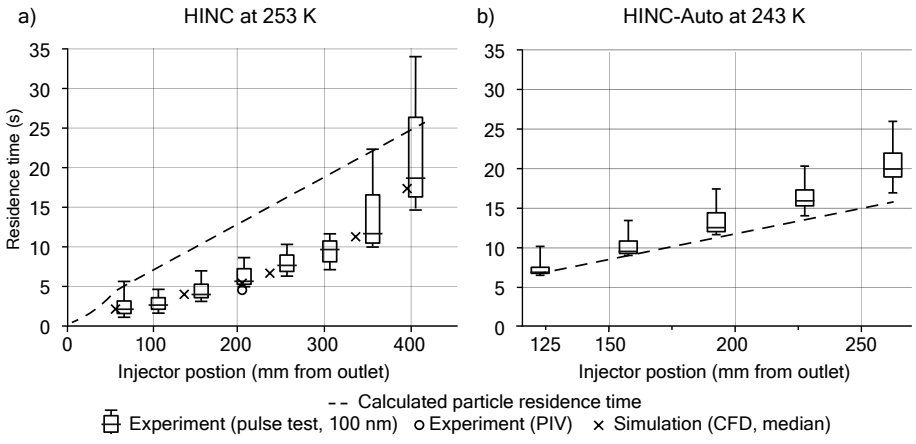

Figure 3. Calculated and measured particle residence time in a) HINC (without mesh) for different injector positions at T = 253 K and b) HINC-Auto (using a mesh to achieve a more uniform flow) at T = 243 K. Box plots from pulse experiments: median with 25/75% quartiles, whiskers: 5/95% quantiles. Median of PIV experiment (circles, T = 288 K) and CFD simulation (crosses, T = 243 K).

2.3.1 Reduction of rewetting duration

Maximizing the time HINC-Auto is sampling ambient air for INPs requires the duration of the rewetting procedure to be minimal. The limiting factor is warming up and cooling down the chamber from the working temperature (i.e. 243 K) to temperatures above the melting point of water (e.g. 293 K) and vice versa. The time to warm up and cool down the chamber is mostly set by the chiller's performance and by the heat capacity of the chamber itself. The new chiller (Lauda PRO RP 290E) had the best performance in comparison to the available products and their parameters, such as cooling power between 290 and 240 K, size, weight and price. Furthermore we decided to minimize the chamber's total heat capacity by machining the walls in aluminum instead of copper. A heat conduction analysis using the Finite Element Method in STAR-CCM+ V13.04.010 revealed sufficient temperature equality $\leq$ 0.02 K at T = 243 K across both walls when changing from copper to aluminum, despite the 70% lower thermal conductivity. The 3D ~~CDF~~ CFD simulation revealed for the supersaturation to need a substantial part of the chamber length to equilibrium to the set conditions. For T = 243 K and S_{w} = 1.04 a 96% equilibration (S_{w} = 1.00) was reached just 20 cm of the sheath air inlets (43% of the entire chamber length in HINC). A faster equilibration allows for a reduction of the chamber length, and subsequently, a further reduction in total heat capacity. To be more time efficient in studying the impact of the chamber length, a numerical 2D diffusion model approach was chosen over 3D CFD simulation. The newly developed 2D diffusion model has been validated with the analytical solution by Rogers (1988) and the 3D CFD simulation (see Figure A4). In order for the supersaturation to equilibrate to the set supersaturation, the temperature as well as the water vapor distribution along the chamber's height have to equilibrate from the initial conditions. Figure 4a shows the equilibration of the supersaturation profile in HINC to be temperature limited when injecting sheath air at $T_{sheath\ air}$ = 298 K with a dew point of T_d = 233 K while the chamber is set to T = 243 K and S_{w} = 1.04. By precooling the sheath air to $T_{sheath\ air}$ = 248 K the chamber can be shortened by 10 cm to facilitate an identical degree of supersaturation equilibration during the final 10 seconds (see Figure 4b). Larger residence times than 10 seconds are prone to hydrometeor sedimentation and are therefore not targeted. Precooling is achieved by blowing the sheath air onto heat sinks, mounted on the cold wall just upstream of the mesh. The mentioned changes and the new chiller decrease the duration of rewetting from 110 min with HINC to 50 min with HINC-Auto.

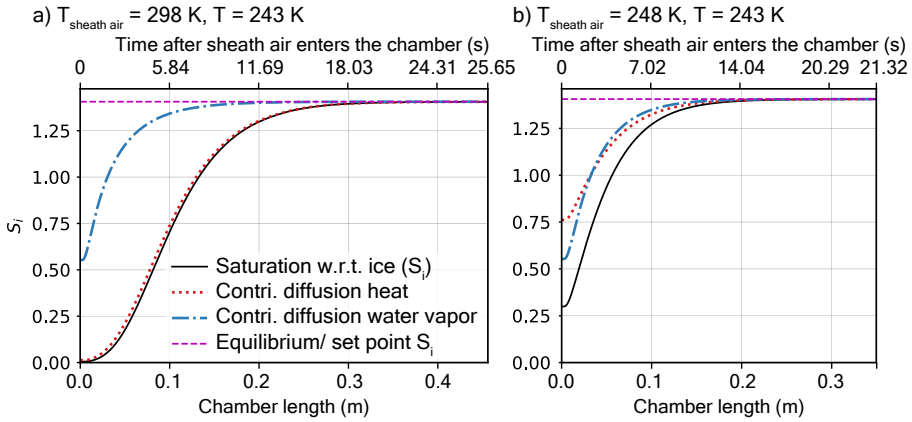

Figure 4. Simulated ice supersaturation development along the chamber's center lamina at T = 243 K and contributing factors diffusion of heat and water vapor for a) ~~original chamber length of 45.7 cm and sheath air injected at ambient temperature (~~$T_{sheath\ air}$ = 298 K (original length) and b) ~~with 10 cm reduced chamber length and precooled sheath air to~~ $T_{sheath\ air}$ = 248 K (allowing for the chamber length to be reduced by 10 cm).

2.3.2 Change of the axis of rotation during the rewetting procedure

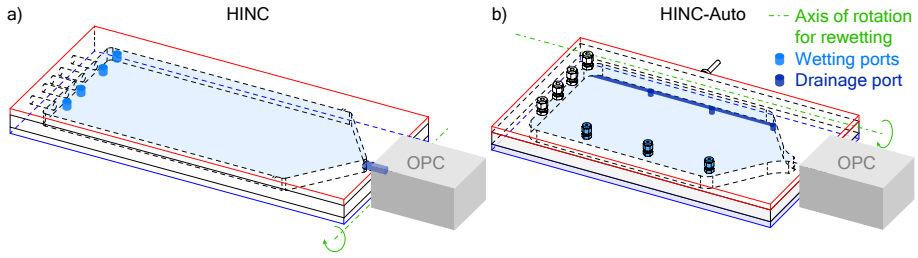

Figure 5. Illustration of the axis of rotation, location of wetting and drainage ports on a) HINC and b) HINC-Auto.

When rewetting HINC, the ~~optical particle counter (OPC)~~ OPC has to be disconnected from the chamber's outlet to allow excess water to drain. HINC is thereby tilted 23° around an axis parallel to the width of the chamber (see Figure 5a). During rewetting HINC-Auto is tilted 25° around an axis parallel to the length of the chamber. This allows for the OPC to stay attached but required 3 additional drainage ports in the bottom wall, located just below the spacer's side wall(see Figure 5b).

2.3.3 Software

The chamber is controlled via a newly developed guided user interface programmed using Python 3.7 and corresponding open source packages. The postprocessing of INP concentrations is done in real time. HINC-Auto can be accessed and controlled remotely if ~~a~~ an internet connection is available on site~~.~~, however this is not a requirement for autonomous operation. A

screenshot of the guided user interface with comments on the basic parameters a user can set is shown in the appendix (A7 -A11).

2.4 Derivation of the INP concentration

Immersion mode INP measurements are performed by sampling at T = 243 K and S_w = 1.04. At these conditions, CCN should activate to supercooled droplets, and INPs, which are active at 243 K, form ice crystals. The size of the hydrometeors exiting the chamber is used to differentiate between liquid droplets and ice crystals because ice grows to larger sizes at the prevailing conditions ($S_i \gg S_w$). Differential measurements between the total aerosol inlet and immediately downstream of the chamber with an OPC were used to determine particle losses. The transmission fraction of ambient particles $\geq$ 2 µm through the tubing and the ~~warm, dry chamber~~ dry chamber (both walls held at 293 K) on the JFJ is 33%. No ambient particles $\geq$ 3 µm were transmitted.

~~Diffusional growth calculations at the described T and S_w conditions predict a maximum droplet size of d = 4.99 m (Zurich, 965 hPa, τ = 9.1 s) and d = 4.24 m (JFJ, 645 hPa, τ = 6.1 s) for large particles with an initial diameter of~~ Therefore, to assess the maximum size of droplets in the following diffusional growth calculations a maximum initial radius of d_0 = 2 µ~~m. However, when accounting for the supersaturation equilibration within the chamber using the 2D-Diffusion model,~~ m is used.

Diffusional growth calculations (Rogers and Yau, 1989) with set fixed T (e.g. constant at 243 K) and S_w (e.g. constant at 1.04) conditions overestimate the final hydrometeor size at the chamber exit since the calculation assumes a constant supersaturation to be maintained for the entire time the particle passes through the chamber. In reality, the ~~calculated diffusional growth along the particle's trajectories should result in hydrometeors of smaller sizes~~saturation in the particle stream needs to equilibrate to the set conditions, thus, the particles are exposed to a lower saturation for the first few seconds (see Figure A4). The 2D diffusion model provides an estimate of the real T and S_w when using the diffusional growth calculations by Rogers and Yau (1989). For an ~~identical initial radius~~initial diameter of d_0 = 2 µm, liquid droplets are calculated to grow to a maximum size of ~~d~~ d_{liq} = 3.31 µm (Zurich, 965 hPa, τ = 9.1 s) and ~~d~~ d_{liq} = 2.36 µm (JFJ, 645 hPa, τ = 6.1 s). Measurements of a highly hygroscopic aerosol, ammonium nitrate with an initial mobility diameter of d_m = 200 nm (for the sample preparation see Section ~~results/validation~~3.2) show the onset of cloud droplets (no ice crystals since $T > 235$ K) in the $\geq$ 3 µm-size bin at S_w = 1.038, as seen in Figure 6a, and support the calculated maximum size of 3.31 µm at S_w = 1.04. The impact on the final diameter for an initial size of $d_{0_{0.2}}$ = 200 nm compared to $d_{0_{2.0}}$ = 2 µm is ~~-0.414~~ 0.63 µm (~~$d_{2.0}$~~ $d_{liq_{2.0}}$ = ~~4.99 vs. $d_{0.2}$~~ 3.31 µm vs. $d_{liq_{0.2}}$ = ~~4.57~~ 2.68 µm at 965 hPa and τ = 9.1 s). If the INPs activate as soon as ice saturation is exceeded, the ice crystals grow to $d_{ice_{2.0}}$ = 7.77 µm, $d_{ice_{0.2}}$ = 7.51 µm at 965 hPa and τ = 9.1 s and $d_{ice_{2.0}}$ = 7.66 µm (JFJ, 645 hPa, τ = 6.1 s). Therefore, for experiments performed at T = 243 K and S_w = 1.04, all particles detected in the size bin $\geq$ 4 µm are considered to be ice crystals formed on INPs. Figure 6b shows a measured activated fraction (AF) curve of ambient air on the JFJ during a high INP concentration period (7:05 22. March 2020, UTC). AF is the ratio of all particles, that are detected in the indicated size bin, to all sampled particles, measured with a CPC within the sample flow. The onset of cloud droplets in the $\geq$ 0.3 µm size bin exactly at S_w = 1 demonstrates the accuracy of HINC-Auto. At S_w = 1.13 an observed steep increase in AF in the $\geq$ 3 µm-OPC size

bin indicates droplets only grew larger than 3 µm at this S_w. Compared to the ammonium nitrate measurements performed at Zurich, a delayed activation is observed. This is expected because of the decrease in ambient pressure, which results in shorter residence times, and the ~~less pronounced~~ much lower hygroscopicity of ambient particles at the JFJ compared to ammonium nitrate. The signal visible in the $\geq$ 4 µm-OPC size bin comes from INPs, which nucleate and grow to ice crystals at $S_w \geq 1.028$ ($S_i \geq 1.378$). This validates the calculations above that at S_w = 1.04 droplets cannot grow to sizes $\geq$ 4 µm but ice crystals can supporting the use of the $\geq$ 4 µm size bin to detect ice crystals.

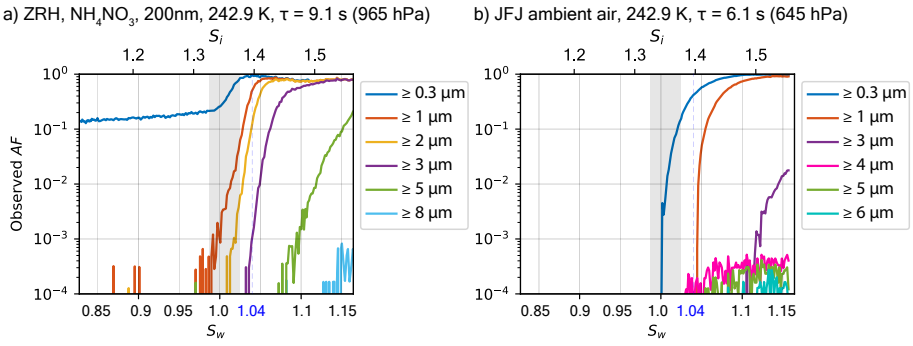

Figure 6. Activation curve at T = 243 K for a) ammonium nitrate, sampled at Zurich and b) ambient air, sampled at JFJ during an period with enhanced INP concentrations. Both measurements were performed with HINC-Auto with an identical injector position, but resulted in a shorter particle residence time (τ) at the JFJ compared to Zurich because of the reduced ambient pressure. Grey shading refers to chamber uncertainty (see Section 3.1 for details).

False positive counts can arise from large particles other than ice nucleated on an INP. Dominant false positives arise from frost grown on inner chamber surfaces which break off and get carried with the prevailing airflow until exiting the chamber, where they are detected by the OPC. To assess and correct the measurements for these false counts, before and after a sampling period of 15 min a background measurement of 5 min is performed. During the background measurement the sample air is directed through a HEPA filter before being sampled in the chamber. The mean time-normalized background counts before and after each INP measurement in the $\geq$ 4 µm bin are subtracted from the $\geq$ 4 µm-OPC counts during the INP measurement before the conversion to std L min^{-1}. The ~~limit of detection (LOD)~~ INP concentration is calculated as follows:

$$INP\ concentration = \left(\frac{\sum INP\ counts}{\sum N_{INP\ samples}} - \frac{\sum BG\ counts}{\sum N_{BG\ samples}} \right) \frac{1}{V t_{OPC}} \quad (1)$$

~~Where~~ where $\sum INP\ counts$ is the sum of all counts (particle number) in the $\geq$ 4 µm OPC size bin during the INP measurement, $\sum N_{INP\ samples}$ is the total number of OPC intervals during the INP measurement, $\sum BG\ counts$ is the sum of the background counts (particle number) in the $\geq$ 4 µm OPC size bin before and after the ~~measurement~~INP measurement while sampling through a particle filter, $\sum N_{BG\ samples}$ is the total number of ~~OPC intervals with duration t_{OPC} in seconds used to count all background counts~~ background OPC intervals before and after the ~~measurement,~~ INP measurement, t_{OPC} is the duration of each OPC interval in minutes (here 5 sec, thus 5/60 min), and V is the sample flow rate, here V = 0.283 std L

min^{-1}. As the volume flow through the OPC is controlled by the MFC in std L min^{-1}, the resulting INP concentration is INP std L^{-1}.

The limit of detection (LOD) is calculated as follows:

$$LOD = \frac{\sqrt{\sum BG\ counts}}{\sum N_{BG\ samples}} \frac{1}{V t_{OPC}} \quad (2)$$

where the LOD is in std L^{-1}. If over a period of 120 OPC background sampling intervals with a duration of 5 seconds each a total of 3 counts where detected in the $\geq$ 4 µm OPC size bin, the LOD would be = 0.612 std L min^{-1} ($\sum N_{BG\ samples}$ = 120, ~~here~~ t_{OPC} = 0.083 min, $\sum BG\ counts$ = 3, V = ~~2.83~~ 0.283 std L min^{-1}). The stated LOD provides a 62.3% (1 σ) confidence interval. The minimum detectable concentration (MDC~~,~~) is 1 count ~~) for a~~ (particle) in the $\geq$ 4 µm OPC size bin over a 15-minute INP measurement with a sample flow rate of 0.283 std L min^{-1}~~over 15 minutes is~~, which equals MDC = 0.236 std L^{-1}.

2.5 Quality control

The algorithm to derive the INP concentration also performs a quality control. When a deviation from the set conditions (see below) is observed, the data is stored normally but a flag is added to the measurement. The evaluation of the flag and a potential exclusion of the data needs to be done by a researcher during post processing. Deviations are flagged (i) if the mean temperature of either wall is off by more than a predefined value (here $\pm$0.15 K), (ii) one of the two MFCs reports a deviation between the set and the measured flow rate by more than $\pm$50 std mL min^{-1}, (iii) the chiller reports an error, (iv) the pressure within the chamber is different by more than 50 hPa from the ambient pressure or (v) the water reservoir, used to rewet the chamber walls, is below a defined threshold (approx. 100 mL).

3 Results

3.1 Accuracy

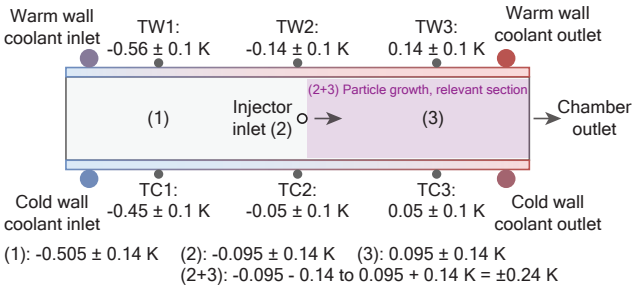

Figure 7. Schematic of uncertainty in temperature measurement showing a side view of HINC-Auto. TW and TC refers to one of six thermocouples installed on the warm wall and cold wall, respectively. Positions (1), (2), (3) and (2+3) indicate the temperature uncertainty of the center lamina. . For each of the positions (1), (2), and (3) we have the ± 0.1 K form the warm and ± 0.1 K from the cold wall thermocouple, thus $\pm\sqrt{0.1^2 + 0.1^2}$ K = ±0.14 K

Four main parameters characterize the INP concentration measured: temperature, supersaturation, particle count and volume flow. The thermocouples have an uncertainty of ±0.1 K and are calibrated measuring the melting of H_2O and Hg, in close agreement with the ITS-90 (the official protocol of the international temperature scale). The measured relative (compared to set point T) temperature variation across the warm and cold wall is ~~± 0.35 K and ± 0.25~~ -0.56 / +0.14 K and -0.45 / +0.05 K at T = 243 K and S_w = 1.04, respectively (see Figure 7). However, on each wall only the two thermocouples close to the injector (TW2/TC2) and the chamber outlet (TW3/TC3) are used to calculate the mean wall temperature. The relative variation therefore decreases to ±0.14 K (at the warm wall) and ±0.05 K ~~at~~ (at the cold wall) for a center nominal temperature of T = 243 K ~~and~~ at S_w = 1.04~~on the warm and cold wall, respectively~~. In either case, the temperature increases in the direction of the air flow, because of the parallel-flow setup of the cooling liquid (see Figure 2b). Subsequently, the uncertainty of the center lamina is -0.095 K for the relative variation plus ±0.14 K for the thermocouples uncertainty at location (2) and 0.095 K ± 0.14 K at location (3). Therefore, the resulting total temperature variation in the ~~center~~ section relevant for particle nucleation or activation and growth between the two cooling walls is ~~$T\pm$~~ T ±0.24 K. The accuracy of the supersaturation within HINC-Auto relies indirectly on the measured temperature, too, since the wall temperatures define the supersaturation. In addition, the vertical position of the aerosol layer determines the T and S experienced by the particles. Thus, the temperature uncertainty translates together with the maximal displacement of the particles within the center lamina with a sheath to sample flow ratio of 9:1 resulting in a supersaturation uncertainty of S_w +0.007 and ~~- 0.009~~ -0.009 and a total temperature uncertainty of ±1.11 K at nominal T = 243 K and S_w = 1.04. This corresponds to a experienced range of $1.03 \leq S_w \leq 1.05$. ~~The~~ According to the manufacturer, the used OPC can ~~distinguish and size bin~~ count 4995 ~~individual~~ particles per second~~with an~~, and simultaneously classify their optical size and place them in one of 6 user-defined size bins, with an overall accuracy of ±10% to the calibrated aerosol. The sheath air MFC has a standard deviation of σ = 1.07%, and the MFC downstream of the

OPC a standard deviation of σ = 0.25%. The CPC used for validation experiments has a counting uncertainty of $\pm$10% which yields in a relative uncertainty in the reported *AF* of $\pm$14%.

3.2 Validation

An overview of the validation of HINC-Auto is shown in Figure 8. Ammonium sulfate ($(NH_4)_2SO_4$), ammonium nitrate (NH_4NO_3) and sodium chloride (NaCl) were sampled from a aqueous solution with 0.1 mol L^{-1}, atomized, dried using a diffusion dryer to $S_w \leq 0.002$ at 20 °C and size selected to a mobility diameter d_m = 200 nm by a differential mobility analyzer (DMA, TSI 3082, sheath flow set to 8 L min^{-1}, sample flow 1.3 L min^{-1}). A CPC (TSI ~~3878~~3787) measured the particle concentration in parallel to HINC-Auto to obtain *AF*. The particle concentration was targeted to 200 cm^{-3}. The injector position in HINC-Auto was kept constant yielding in between τ = 8 (273 K) and 10 seconds (218 K) residence time, depending on the temperature of the mid lamina. The experiments were conducted with constant mid lamina temperature while the super saturation is increased with ΔS_w = 0.02 min^{-1}. The onset of activation in the 1 µm-channel is reported for when the signal exceeds the background noise levels.

NH_4NO_3 is used to test cloud droplet formation at $T \geq 235$ K and homogeneous freezing of solution droplets at $T \leq 235$ K. Cloud droplet formation within the uncertainty range of HINC-Auto is detected at water saturation for 235 K $\leq T \leq$ 263 K. At the lower end of the temperature spectrum, the activation onset is more sudden (see Figure A5) and starts lower than water saturation. For homogeneous freezing at 233 K the activation is steep at S_w = 0.97, 0.017 lower than the parameterized homogeneous freezing onset of solution droplets for d_0 = 200 nm and $J = 10^{10}$ $cm^{-3}s^{-1}$ (Koop et al., 2000b), but within the theoretically reported value considering uncertainty. At 228 and 222 K, the measured activation agree well with the the parameterized homogeneous freezing onset. The deliquescence of ammonium sulfate ($(NH_4)_2SO_4$) was observed at S_w = 0.88 (at 234.9K) to 0.86 (at 245.1K) within the range of uncertainty of literature values (Braban et al., 2001) as shown in Figure 8. The deliquescence of sodium chloride (NaCl) lies within the range of uncertainty of measured values by Koop et al. (2000a).

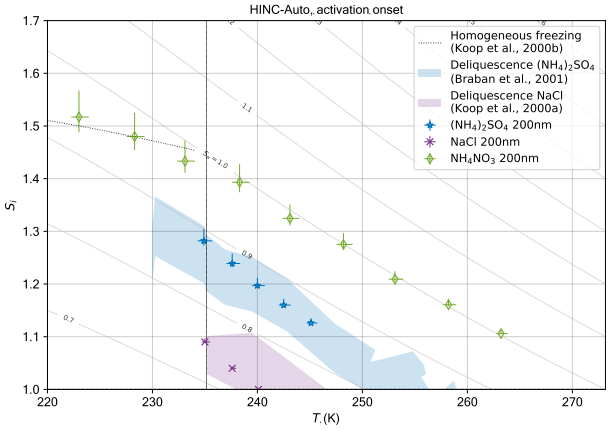

Figure 8. Data from experiments in HINC-Auto and comparison to values from literature for cloud droplet formation and homogeneous freezing onset with ammonium nitrate, and deliquescence of ammonium sulfate and sodium chloride. Reported is the activation onset when the signal increases above the background noise levels. Dashed line: homogeneous freezing onset of solution droplets for d_0 = 200 nm and $J = 10^{10}$ cm^{-3}s^{-1} (Koop et al., 2000b).

3.2.1 Improvement in precision

Figure 9 shows the activation curves of ammonium nitrate ~~experiments~~ size selected to a mobility diameter of d_m = 200 nm and measured at T = 233 K ~~performed~~ with HINC-Auto compared to measurements performed with HINC. The sample preparation is as described ~~above~~ in section 3.2 for both chambers ~~and the~~ with a lower DMA sheath flow of 5 L min^{-1} and a higher sample flow of 1.6 L min^{-1} to feed both chambers and the CPC. This resulted in a broader transfer function within the DMA and consequently more larger and multiple charged particles penetrating the size selection. Due to the hygroscopicity of ammonium nitrate, the multiple charged particles are detected in the $\geq$ 1 μm OPC size bin after hygroscopic growth at S_w $<$ 0.98. In comparison, measurements in section 3.2 and Figure A5 use a narrower DMA transfer function and show a lower activated fraction below $S_w < 0.98$ than in the experiment with the broader transfer function. The injector position was chosen to result in residence times of $\tau \approx 9$ seconds. The standard sheath to sample flow ratio ~~was~~ of HINC-Auto was adjusted to 12:1 ~~for both chambers~~ to be equal to the ratio used in HINC in order to compare the performance of the two chambers (note that the standard sheath to sample flow ratio of HINC-Auto is 9:1. See Section 2.2). HINC-Auto shows an improved ~~reproducibility~~ precision compared to HINC. We attribute the improvement to the use of the mesh and, subsequently, the more uniform flow within HINC-Auto compared to HINC without the mesh. For measurements in the field with HINC, a defined supersaturation (e.g. S_w = 1.04), temperature and OPC-size bin (e.g.$\geq$ 4 µm) is used to quantify INPs. Therefore, fluctuations in the activation ~~reproduciblity~~ precision of the $\geq$ 4 µm size bin can lead to uncertainties in INP concentrations. In the example of HINC, this is equivalent to more than one order of magnitude, thus an improved ~~repeatability~~ precision improves the quality of the INP measurements. In addition, particle sedimentation, as expected by theory (see ~~Section~~ section below), is visible in the activation curves of HINC-Auto at $S_w \geq 1.02$ (see Section 3.2.2).

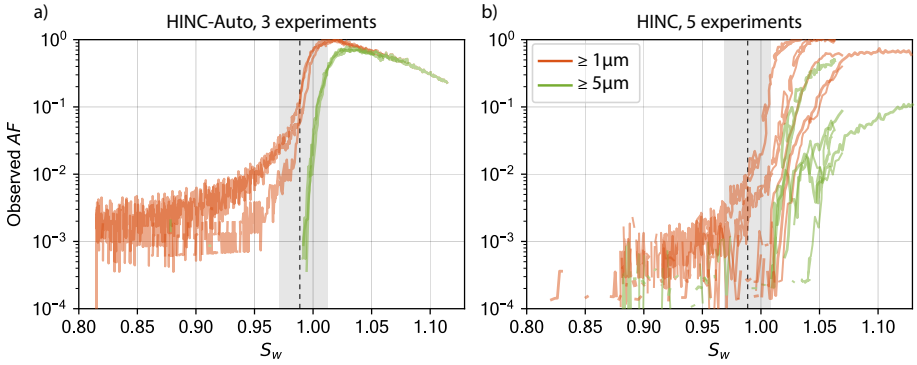

Figure 9. Activation curves of ammonium nitrate in HINC-Auto (a) and HINC (b) at T = 233K with identical particle residence times ~~.~~of $\tau \approx 9$ sec.; the vertical dashed line indicates the expected homogeneous freezing onset of solution droplets for d_0 = 200 nm and J =10^{10} $cm^{-3}s^{-1}$ (Koop et al., 2000b). Sizes indicate what fraction of all particles entering the chamber grow to or beyond the indicated size. Grey shading refers to chamber uncertainty (see Lacher et al. (2017) for details on HINC and Section 3.1 for details on HINC-Auto).

3.2.2 Sedimentation study

The 2D diffusion model can also be used to calculate the diffusional growth of liquid and solid hydrometeors and their subsequent sedimentation characteristics. An example is given in Figure 10a and compared to an experiment of silver iodide (AgI, Figure 10b) at T = 243 K with a residence time of τ = 13.7 sec at p = 965 hPa. AgI samples were prepared by aqueous solutions of 0.01 mol L^{-1} of potassium iodide and silver nitrate, where the silver nitrate solution was slowly added to the potassium iodide under constant stirring. This procedure favors the formation of β-AgI over α-AgI (Brauer, 1965). After resting for 60 min, the top 80% (consisting only of a clear solution) of the yellow suspension was decanted and the equivalent of removed volume was added in ultra pure water. A brief swivel lofted the settled precipitate. The decanting procedure was repeated twice. The suspension was atomized, dried using a diffusion dryer to $S_w \leq 0.008$ at 20 °C and size selected to d_m = 100 nm by a DMA. For the simulation, the ~~ice active fraction (*FF*)~~ fraction of INPs has been set to 15% for the simulation to agree best with the ~~*FF* observed. The *FF*~~ experiment. The fraction of INPs depends on the fraction of ice active β-AgI particles within all particles (Marcolli et al., 2016), which also contain ice inactive α-AgI particles and cannot be deduced by the 2D diffusion model, and therefore, needs to be prescribed. The model uses the size distribution after the DMA measured by a Scanning Mobility Particle Sizer (SMPS) setup (DMA, TSI 3081, with CPC, TSI 3772) as input for the particle initial sizes and also places the particles (N = 1000 for each, INPs and CCN) at uniformly distributed vertical positions within the sample lamina. The model assumes instant activation of the particles as soon as ice or water saturation are reached. Also Köhler-theory is not implemented. Ice crystals are assumed to be spherical.

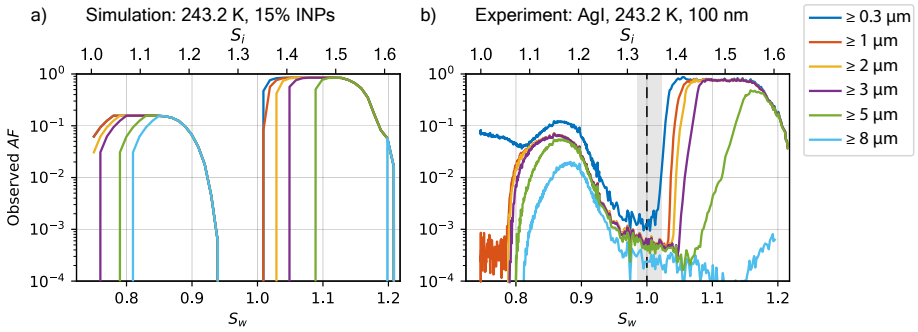

Figure 10. a) Simulated ~~activation~~ activated fraction curve as a function of S_w with a ~~frozen~~ prescribed fraction ~~*FF*~~ of INPs of 15% for $S_w \leq 1$ and b) measured ~~activation curve~~ activated fraction of d_m = 100 nm silver iodide (AgI) particles, both at T = 243 K, with a particle residence time of τ = 13.7 sec at p = 965 hPa. Sizes stated in the legend indicate what fraction of all particles entering the chamber are activated and grow to or beyond the indicated size. Grey shading refers to chamber uncertainty around S_w = 1.0 (see Section 3.1 for details).

The model can capture the general trend of the experiment. The rapid onset of ice formation at $S_w \leq 0.8$ is not reproduced because this depends on the nucleation rate of the substance, which is neither parameterized nor simulated using molecular dynamics or similar approaches. However, the simulation demonstrates an upper bound of possible sizes, which is in agreement with the experiment. Where the ice growth is limited by the amount of supersaturation required for diffusional growth, e.g. at $S_w \geq 0.81$, the transition of ice crystals growing to a size ≥ 8 µm is reproduced well. The sedimentation of the ice crystals is observed at $S_w \geq 0.87$ while the simulation predicts $S_w \geq 0.86$. The onset of liquid droplets is identical in the experiment for sizes ≤ 3 µm, and delayed for larger sizes. Water vapor depletion is not likely the cause because running the experiment with a sample concentration of 20 or 1200 particles cm^{-3} compared to the original 200 particles cm^{-3} did not alter the slow growth of hydrometeors ≥ 5 µm. We expect the delay to be present because of the missing implementation of Köhler-theory. The AF in the experiment as well as in the simulation is leveling off at AF = 0.85 for $1.02 \leq S_w \leq 1.13$. Ice crystals ($\approx$ 15 % in the experiment) and supercooled droplets are continuously formed at these supersaturations, but ice crystals grow to such large sizes that they sediment and are not detected at the outlet anymore. Therefore, maximum droplet activation of all non-ice active particles is observed in this region. The sedimentation of droplets is observed delayed at $S_w \geq 1.16$ compared the model output at $S_w \geq 1.13$. This is likely a result of the delayed onset of liquid droplet formation seen in the experiment. While increasing the supersaturation the droplets remain too small, thus their size-dependent settling is delayed, too.

3.2.3 INP measurement

To assess HINC-Auto's capability of fully automated INP measurement, ~~Nx~~ NX Illite was sampled in a controlled laboratory environment. The goal of this experiment is to assess how reliablly INPs can be detected over different INP concentrations and what their impact is on the ice layer endurance, thus deciding which rewetting intervals are needed and to test the overall automation of the chamber. HINC-Auto was, therefore, run autonomously except for a change in when to trigger the rewetting sequence. Using the software user interface, a command was sent to the chamber after the chamber was presumed to have

run dry. This has been inferred based on the decay of the reported INP concentrations. For the experiment, ~~Nx~~ NX Illite was dry dispersed by a rotating brush generator (PALAS, RBG 1000) into a stainless steel aerosol chamber with V = 2.78 m^3, initially filled with dry, pure nitrogen. The volume within the aerosol chamber was actively stirred with a gold-plated fan (30 cm diameter). The observed particle number size distribution was 30 - 1000 nm (see Figure 11a). A common sample line from the aerosol chamber feeds a two way flow spitter, which connects HINC-Auto and a CPC (TSI 3778) using tubing with identical length and diameter. A burst of ~~Nx~~ NX Illite was initially added to the aerosol chamber and continuously diluted by sampling 0.883 std L min^{-1} (0.283 std L min^{-1} for HINC-Auto and 0.6 std L min^{-1} for the CPC) and adding 1.0 std L min^{-1} of dry N_2. An additional bypass valve allowed to vent the excess N_2 before entering the aerosol chamber. HINC-Auto was run at mixed-phase cloud condition at T = 243 K and S_w = 1.04 to sample in the immersion freezing mode with a sheath to sample flow ratio of 9:1 and a residence time of $\tau \approx 8$ seconds. The chamber measured intervals of sample aerosols for 15 min and filtered background for 5 minutes. Figure 11b shows the measured INP and particle concentrations during the course of the experiment. Since the initial burst of ~~Nx~~ NX Illite is suspended in dry, inert nitrogen, it is expected for the ice active fraction to remain fairly constant or decrease slightly over time. A slight decrease is expected when larger particles, which tend to be more ice active because of the higher surface area, sediment within the tank sooner than small particles. A SMPS setup (DMA, TSI 3082, with CPC, TSI ~~3878~~3787) measured the size distribution at the beginning of the experiment and after 62 hours (see Figure 11a). ~~The for~~ For the initial scan (solid line) the sheath flow was set to 5 L min^{-1}, and for the second scan to 2 L min^{-1} (dashed line). At a lower sheath flow rate, the SMPS scan shifts to cover a larger range of particle sizes while limiting the scanning range at smaller particle sizes. Both measured size distributions were similar with a small shift towards larger particles for the later scan. This ~~is contradicting our assumption and the lower sheath flow rate of the DMA for the second compared to the first measurement could be the reason~~contradicts the assumption of large particles sedimenting more quickly than small particles, thus shifting size distribution towards smaller particle sizes with time. A reason could be due to particle coagulation in the stainless steel aerosol chamber, which causes the observed shift in size distribution towards larger particle sizes. The measured INP concentrations show a systematically repetitive trend: After each rewetting sequence the ratio between particle and INP concentration is approximately 1:1000. During the operation of the chamber the ratio remains fairly constant and decreases after some time. We expect the decrease to coincide with the depletion of the top wall ice layer. The higher the particle number concentration (N), the sooner the decrease is expected (due to consumption of water vapor mass), and observed. For atmospheric relevant conditions at the JFJ with 400 $cm^{-3} \leq N \leq 1000$ cm^{-3} the drop occurs after 8.5 hours, for 95 $cm^{-3} \leq N \leq 200$ cm^{-3} after 13 hours. N is expected to contribute more in water vapor depletion than the INP number concentration because approximately 1000 times as many particles grow to liquid droplets of a size of $\approx$ 1.3 µm than INPs grow to $\approx$ 4.7 µm. At particle concentrations $\leq$ 30 cm^{-3} and INP concentrations $\leq$ 30 std L^{-1} the INP concentration starts to show noise which increases in relative magnitude with decreasing particle concentrations. A running mean of 4 subsequent measurements decreases the noise and allows the particle to INP ratio to remain until $\approx$ 6 INP std L^{-1}. Based on the above experiment ~~, we chose a rewewtting time of 10~~ we choose a rewetting time of 8 hours for field applications ~~(Section 3.3)~~in remote areas such as Jungfraujoch.

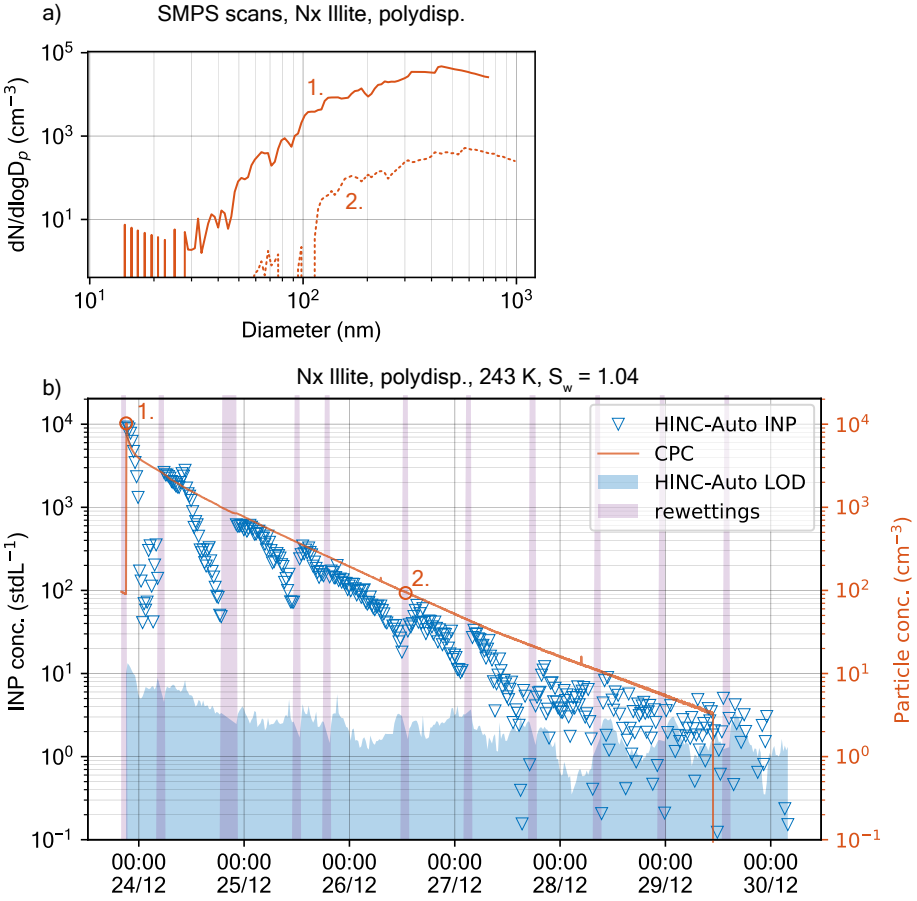

Figure 11. INP concentration in HINC-Auto as a function of time and ~~Nx~~ NX Illite particle concentration. a) SMPS retrieved particle size distribution at time 1 (solid line) and 2 (dashed line). The DMA sheath flow was set to 5 (solid line) and 2 L min^{-1} (dashed line). b) Measured INP and particle concentrations within the aerosol tank.

3.3 Application

The automation of HINC-Auto was tested during a field campaign in August 2019 on the JFJ. In this time, HINC-Auto was operational for 169 out of the 177 available hours (95.5%) and measured 463 measurements-background sequences of a duration of 20 minutes each (see Figure 12a). The maximum measurement coverage with HINC in a time window of 177 hours during previous field campaigns was 191 measurement sequences (see Lacher et al., 2018), also 20 minutes in duration (103 hours, 58%, see Figure 12b). The automation shows a clear improvement in the continuity of the measurements. However, during the field campaign the LOD of HINC-Auto was appreciably higher than the LOD of HINC during previous field campaigns (median LOD HINC-Auto: 3.1 std L^{-1}, HINC: 1.25 std L^{-1}). Design changes implemented in a second field campaign started in February 2020 resulted in a median LOD of 1.37 std L^{-1}. ~~In the~~ It was observed that ice crystals and frost deposited within the cavity of the chamber outlet. We assumed for supercooled liquid droplets, which make up the

majority of the hydrometeor population exiting the chamber, to impact on the surfaces where the Swagelok fitting (to connect the OPC) is inserted into the PVDF frame. The change in inner diameter from the cavity within the PVDF frame (d_i = 10.2 mm) to the fitting (d_i = 3.3 mm) is like a step. The design changes included using a conical drill bit (20°) to smoothen the connection between the chamber outlet and the fitting. In addition, the Swagelok fitting is warmed with a 10 W heat pad during the rewetting procedure to support the evaporation of residual condensate or molten ice that does not drain due to gravity while the chamber is tilted. In the first month the chamber was operational for 698 out of 720 available hours (97.0%). A broken membrane of the recirculating pump caused 10 hours of downtime, the measurement of ramps at the beginning of the campaign resulted in 7 hours when the chamber was not performing INP measurement sequences. The remaining 5 hours were due to multiple software glitches which were fixed. In March 2020, HINC-Auto was operating more reliably with a total downtime of 3 hours because of software bugs. Bug fixes were implemented and let to an operation without any downtime in April 2020. Continuous INP measurements of HINC-Auto at the JFJ are planned to proceed. Live data can be accessed at https://www.psi.ch/en/lac/projects/last-72h-of-aerosol-data-from-jungfraujoch.

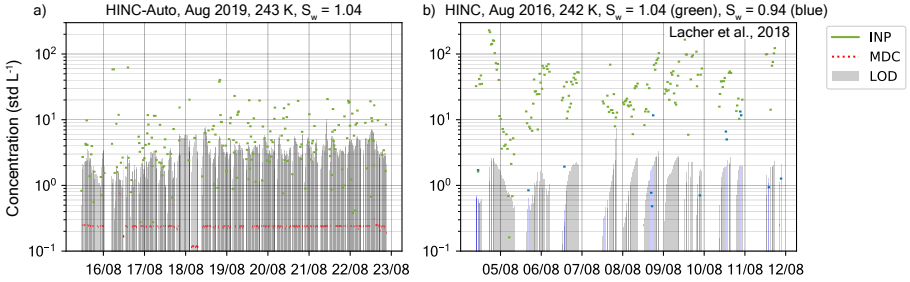

Figure 12. INP measurements at the JFJ over a period of 7 days with a) HINC-Auto at T = 243 K and S_w = 1.04 and b) HINC at T = 242 K and S_w = 1.04 (green markers) or S_w = 0.94 (blue markers) (see Lacher et al., 2018). Green/blue markers indicate the ambient INP concentration, the grey bar indicates the limit of detection (LOD) with a 62.3% (1 σ) confidence interval, red markers indicate measured INP concentrations below the minimum detectable concentration (MDC, 1 count during the sampling time). Every grey bar with a corresponding green/blue/red dot represents one measurement.

4 Conclusions

In this study the automated Horizontal Ice Nucleation Chamber (HINC-Auto) is presented, a continuous flow diffusion chamber to measure atmospheric ice nucleating particle number concentration. During a first field campaign, the chamber was operational fully autonomously for 95% of the time. Over a 90 day period of a second field campaign, HINC-Auto measured INP autonomously for 97% of the time. This time includes INP sampling time as well as periodically reoccurring rewetting procedures. To realize full autonomous operation, the rewetting procedure in HINC was automated. In HINC-Auto, a peristaltic pump remoistens the filter paper that coats the top (warm) wall within the chamber while a linear motor tilts the chamber thereby allowing excess water to drain. The bottom wall passively wets through diffuson of vapour from the cold wall. To maximize the sampling time, the duration of the rewetting procedure was reduced by reducing the warming and cooling time of the

chamber by using a lower thermal mass for the chamber walls. This was done by using aluminium compared to copper and by shortening the chamber. To maintain a well developed relative humidity profile within the sampling section in the shortened chamber, the sheath air is precooled using heat sinks mounted on the cold, bottom wall. Besides the automation, improvements to the flow uniformity were achieved by the integration of a mesh. The resulting activation curves during experiments with relative humidity ramps are steeper in expectation to theory and show a better reproducibility. In addition, the experiments match the predictions of a 2D diffusion model to a high degree. Experiments with HINC-Auto for cloud droplet formation and homogeneous freezing onset with ammonium nitrate, and deliquescence of ammonium sulfate and sodium chloride showed good agreement with values found in literature. HINC-Auto is currently deployed for long-term continuous measurements of INP at JFJ and analysis after a year of data collection will be presented in a follow up study.

Code availability. The code used for simulations presented here is available upon contacting the authors.

Data availability. The data presented in this publication will be made available at DOI: 10.3929/ethz-b-000429220. Note by authors: Data will be made available upon publication

Appendix A

A1 CFD simulations

The CFD simulations were performed using Siemens PLM STAR-CCM+ © V13.04.010. A grid convergence study was conducted prior to the simulations. A 96% convergence of the flow field was observed for the following settings, which were used for all subsequent studies. A tetrahedral mesh with a total count of 9.5×10^6 cells was generated with the surface remesher option and 5 prism layers with a stretching of 1.3. The base mesh size was set to 2 mm with a refinement of 0.25 mm around the injector and the heat sinks and a further refinement of 0.1 mm in the vicinity of the injector's slit. The physics model consisted of 3D turbulent Reynolds-Averaged Navier-Stokes equations, k-ω turbulence model, Lagrangian multiphase with water vapor and air, steady-state, segregated fluid enthalpy, ideal gas, and gravity. Convergence was observed after $\sim$ 2000 iterations with energy-residuals $< 10^{-5}$ as criterion. An unsteady simulation showed no instationary flow behavior and was consistent with the steady-state solution.

A2 Particle Image Velocimetry

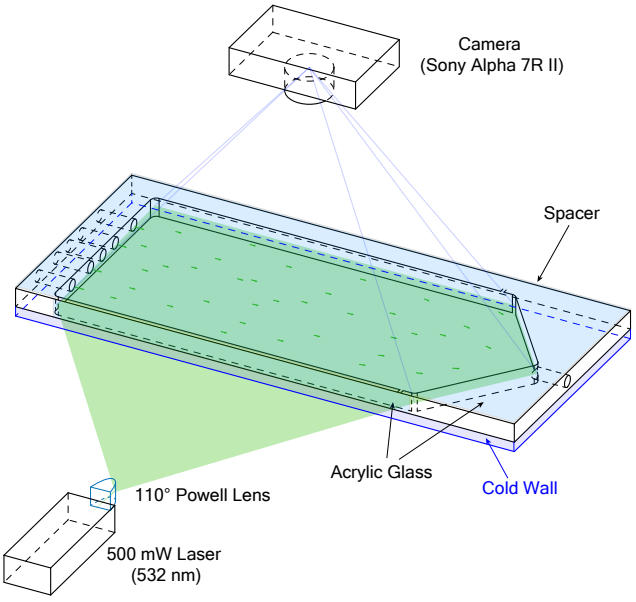

Figure A1. Schematic of the particle image velocimetry experiment with HINC.

Particle image velocimetry (PIV) has been used to validate the CFD-simulations. Figure A1 illustrates the experimental set-up using HINC. Dry ~~Nx~~ NX Illite size-selected particles to a mobility diameter $d_m = 400\ nm$ have been used as tracer. Two experiments were conducted: first, the chamber without the injector. The particles were added to the sheath air. The goal was to sample the overall flow within HINC and deduce the 2D-velocity field. The injector was installed for the second experiment. Here, the areas of interest were to study the impact of the injector on the base-flow within the chamber, as well as the trajectories of non-sedimentating particles as they exit the injector. All results are for the purpose of validating the CFD-simulations. The image sequences were recorded by a SONY Alpha 7R II with a resolution of $\Delta^2_{low} = 3840 \times 2160$ pixel and $\Delta^2_{high} = 1920 \times 1080$ pixel. The camera captured images at $f_{low} = 25$ fps and $f_{high} = 100$ fps. A 500 mW-laser-diode with a wavelength of $\lambda = 532\ nm$ was used as continuous light source. The laser beam is deflected with a K9 110 degree Powell lenses into a straight line, and oriented such, that it illuminates a horizontal plane. The laser's vertical position was controlled by a stepper-motor and could be adjusted with a resolution of 0.05 mm. This allowed to scan the entire chamber and produce a 3D matrix containing the xy-planar velocity components. The laser-facing wall of the CFDC's spacer has been replaced by a planar transparent acrylic glass to allow the laser beam to pass. Also, the top cooling wall has been replaced by clear acrylic glass to allow the camera to capture the illuminated particles. The lower wall was chilled to 279.6 K, while the top acrylic's temperature was at ambient (297 K). The resulting temperature difference of 17.4 K is identical to when the chamber is operated at T = 243 K and $S_w = 1.04$. It is assumed that the absolute temperature has a minor impact on the flow, while it is important to mimic the relative temperature differences since it represents the difference in fluid densities. The post-

processing has been done using PIVlab (Thielicke and Stamhuis, 2014). Fast Fourier Transform linear window deformation technique was used as PIV algorithm with an interrogation area of 128 pixel and a step size of 64 pixel. A second pass an interrogation area of 64 pixel and a step size of 32 pixel followed. Figures A2 and A3 compare the flow field retrieved from the PIV experiments with the CFD-simulations. For the PIV experiments low-settings were used to capture the flow of the entire fluid domain, whereas the $high$-settings were used to extract flow features where the low-settings failed to produce a valid output. Nevertheless, in the areas after the sheath flow outlets the flow velocity was too high to be captures with the $high$-settings. Also, close to the spacer walls, no velocity information could be computed, because of the Fast Fourier Transform window deformation technique. Quantitatively the CFD simulations are able to capture the flow structures measured during the experiment. Quantitatively, the correlation of the u, w-velocity components all voxels resolved by the experiment with the u, w-velocity components of the simulation with identical locations were $r_{HINC} = 0.94$ and $r_{mesh} = 0.95$ for the experiment without and with mesh, respectively. Least correlation was observed in the areas of the sheath flow jets where high flow velocities are present. Also, the simulated particle trajectories were qualitatively stringent with the experiment. Therefore, the CFD simulations were deemed valid.

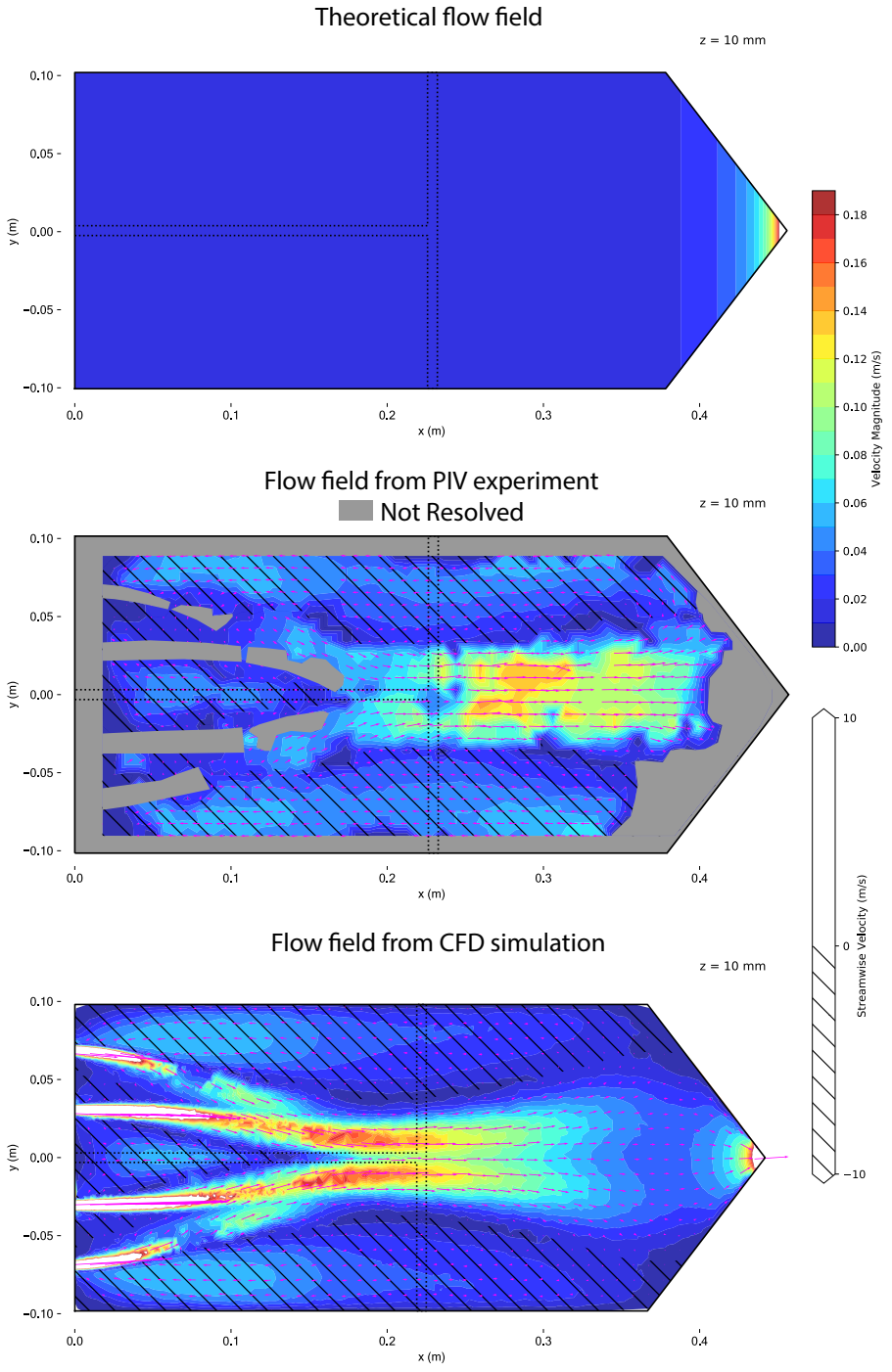

Figure A2. Contour plot of flow velocities magnitudes at a horizontal plane of the HINC cavity at mid-height. The chamber is set to T = 243 K and $S_w = 1.04$. Theoretical flow field (top), flow field measured using PIV (center) and simulated flow field from CFD (bottom). Arrows indicate flow direction, the hatching marks regions with reversed flow. The dashed line represents a possible position of the injector.

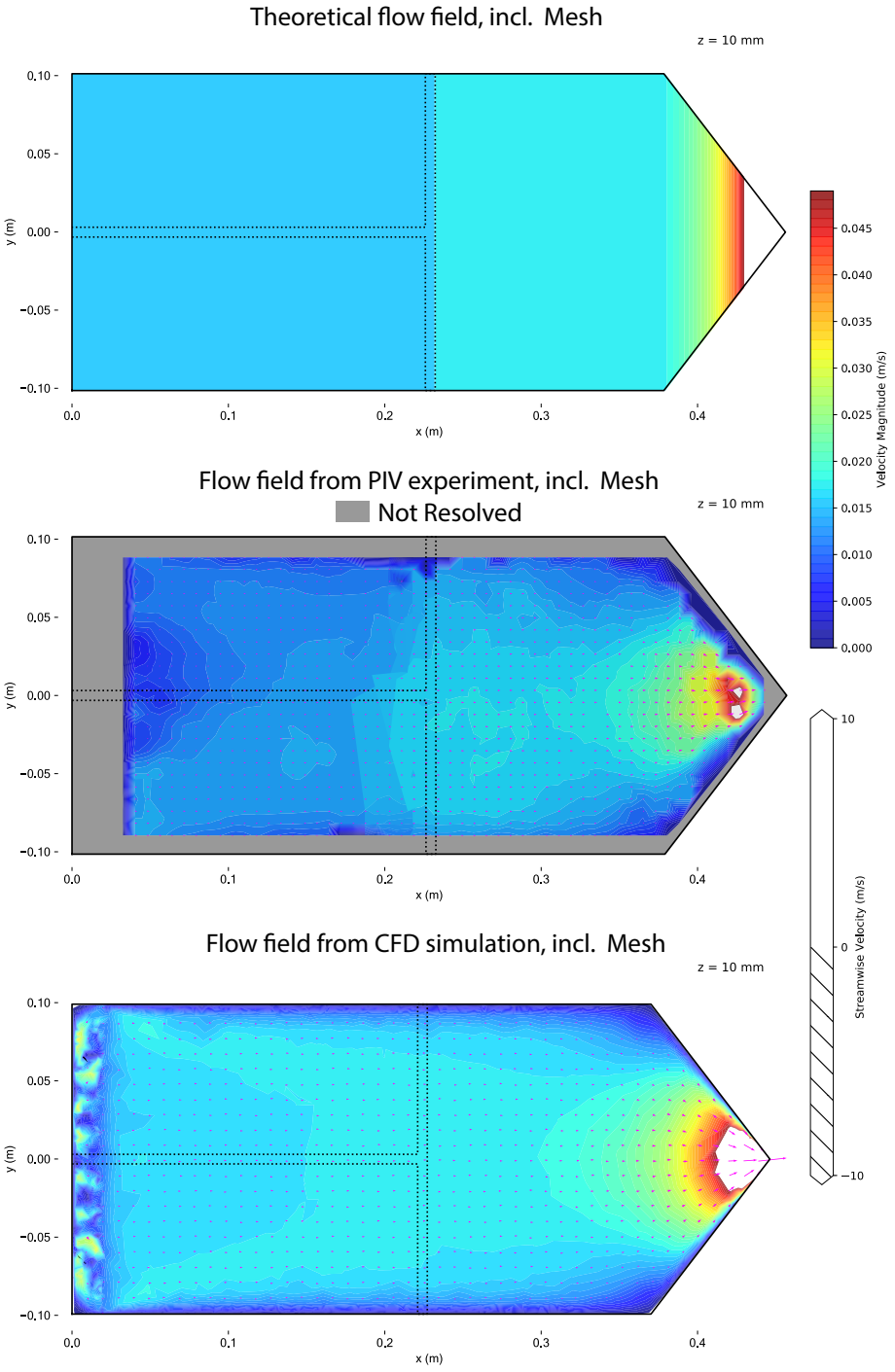

Figure A3. Contour plot of flow velocities magnitudes at a horizontal plane of the HINC cavity at mid-height including a mesh installed at $x_{inj} = 0.022\ m$. The chamber is set to T = 243 K and $S_w = 1.04$. Theoretical flow field (top), flow field measured using PIV (center) and simulated flow field from CFD (bottom). Arrows indicate flow direction, the hatching marks regions with reversed flow. The dashed line represents a possible position of the injector.

A3 ~~2D-Diffusion~~ 2D diffusion model

A numerical diffusion model has been developed to simulate the water vapor saturation field within HINC-Auto. The output of the model is a 2D vertical plane of a horizontal CFDC and its prevailing temperature and water vapor saturation field. Assuming a two-dimensional flow along the chambers length, for the prevalent conditions with Reynolds number $Re = 6.82 \times 10^2$ between two long plates the analytical solution of the Navier–Stokes equations describes a Poiseuille flow according to equations (A1) and (A2):

$$u_{\infty_{bulk}}(x) = \frac{\dot{V}}{A_{yz}(x)} \tag{A1}$$

$$u(x,z) = \frac{3}{2} u_{\infty_{bulk}}(x) \left(1 - \frac{\left(z - \frac{h}{2}\right)^2}{\left(\frac{h}{2}\right)^2}\right) \tag{A2}$$

Where x, y, z are the coordinates along the length, width and height of the chamber. The origin is located on the bottom cooling wall where the sheath-air enters at mid-width. $u_{\infty_{bulk}}(x)$ is the bulk velocity along the chamber's length, V is the preset volume flow of air, $A_{yz}(x)$ is the vertical cross-section of the chamber's cavity which varies along the length of the chamber, u is the stream wise velocity component and h is the total height of the chamber. According to equation (A2) the center lamina has a 50% higher flow velocity than the bulk flow velocity. The particle's theoretical residence time τ_{theory} is calculated using equation (A3):

$$\tau_{theory}(x_{inj}) = \int_{x_{inj}}^{x_{outlet}} \frac{x}{u_{\infty_{bulk}}(x)} dx \tag{A3}$$

Where x_{inj} is the the injector's x-position and the outlet's x-position x_{outlet}.

In CFDCs the temperature and water vapor concentration of the air flow equilibrates from their initial states to form a water vapor supersaturated region. To calculate the sedimentation of particles as well as estimate the particle's final size the two underlying diffusion processes have to be described. Firstly, the heat flux between the warm and cold wall. We assume in accordance to Saxena et al. (1970) no radiation. Although the Nusselt number $Nu = 15.3$ propose otherwise, the calculations are simplified by considering thermal conduction only and neglecting the forced convection. The heat conduction within the ice layer can be neglected (Biot number $Bi = 7.27 \times 10^{-5}$). The calculated numbers are computed for HINC-Auto, the corresponding values of the chamber of Rogers (1988) are $Nu = 22.3$ and $Bi = 1.14 \times 10^{-4}$ for $T_{mid} = 253.15\ K$ and $\dot{V}$ = 4 std L min^{-1}. Besides, the latent heat released or absorbed by the particles or by the wall's ice layer is neglected for calculation of the chamber's internal temperature field. The former is taken into consideration during the diffusion growth calculations (Rogers and Yau, 1989). This leads to the diffusion of heat in air by changing their kinetic energy, according to the heat equation (A4) (Amelin, 1967):

$$\frac{\partial T_{air}}{\partial t} = \frac{\lambda_{air}}{c_{p_{air}} \rho_{air}} \frac{\partial^2 T}{\partial x^2} \tag{A4}$$

Where T_{air} is the temperature of the air, t is the temporal variable, λ_{air} is the thermal conductivity of air, $c_{p_{air}}$ is the heat capacity of air at a constant pressure, ρ_{air} is the density of the air and x is the spatial coordinate.

The second diffusion process is the diffusion of water vapor according to Fick's law (Fick, 1855) in equation (A5):

$$\frac{\partial \mu_{H_2O}}{\partial t} = D_{H_2O/air} \frac{\partial^2 \mu_{H_2O}}{\partial x^2} \tag{A5}$$

Where C_{H_2O} is the concentration of water vapor, $D_{H_2O/air}$ is the diffusivity of water vapor in air and μ_{H_2O} is the chemical potential of the water vapor.

Saxena et al. (1970) states in equation (A5) to use the water vapor concentration C_{H_2O} instead of the chemical potential, yet, it was chosen to use the water vapor partial pressure e in accordance with Rogers (1988). Fundamental theory often suggests the diffusion to be driven by the difference in chemical potential (Sutherland, 1905; Einstein, 1905). Diffusion based on partial pressure or concentration results in different supersaturations than diffusion based on chemical potential. This has has a profound impact on the operating conditions in CFDCs, since the partial pressure is a function of the concentration as well as of the temperature, as seen in the rearranged ideal gas law, (A6), and changes the supersaturation in a non-linear fashion:

$$e = \frac{C_{H_2O} R T}{M_{H_2O}} \tag{A6}$$

~~For the 2D-diffusion~~ To calculate S the equilibrium saturation vapor pressure of water and ice according to Murphy and Koop (2005) is used. For the 2D diffusion model, both heat, and diffusion equations are solved numerically using the forward Euler method. The velocity is prescribed using equation (A2). The 2D fluid domain is modeled using a mesh with a grid spacing of 1 mm (7500 nodes in total). The steady state simulation converged after $\leq$ 100 iterations. Buoyancy has been neglected because it showed to have minor effect on the supersaturation field within horizontal CFDC. The model output has been compared versus a validated CFD simulation as visualized in Figure A4.

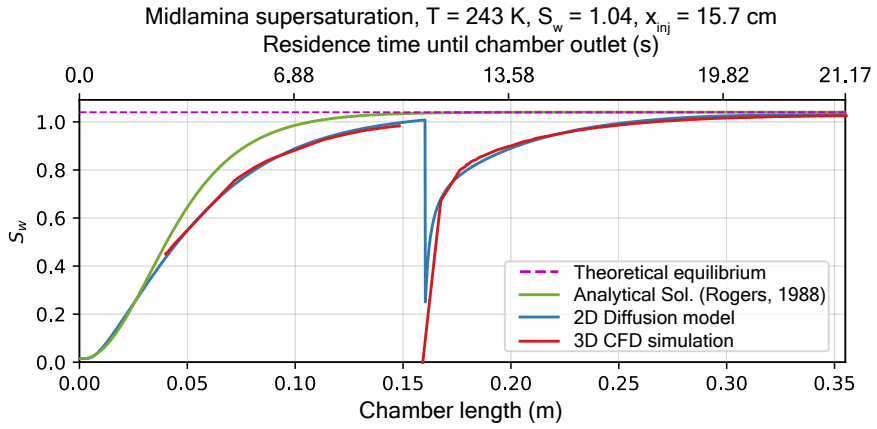

Figure A4. Comparison of the midlamina water supersaturation at T = 243 K, as calculated using the analytical formula (Rogers, 1988), simulated using the ~~2D-diffusion~~ 2D diffusion model and the 3D-CFD simulation. Injector position x_{inj} = 15.7 cm.

Diffusional growth is calculated as according to Rogers and Yau (1989) with the latent heat of sublimation of ice, and latent heat of vaporization of supercooled water according to Murphy and Koop (2005). T and S are variable and feed in from the 2D diffusion model corresponding to the particle's current horizontal and vertical position within the chamber. The diffusional growth of the hydrometeors assumes activation when saturation with respect to ice or water is exceeded.

A4 Ammonium nitrate experiments

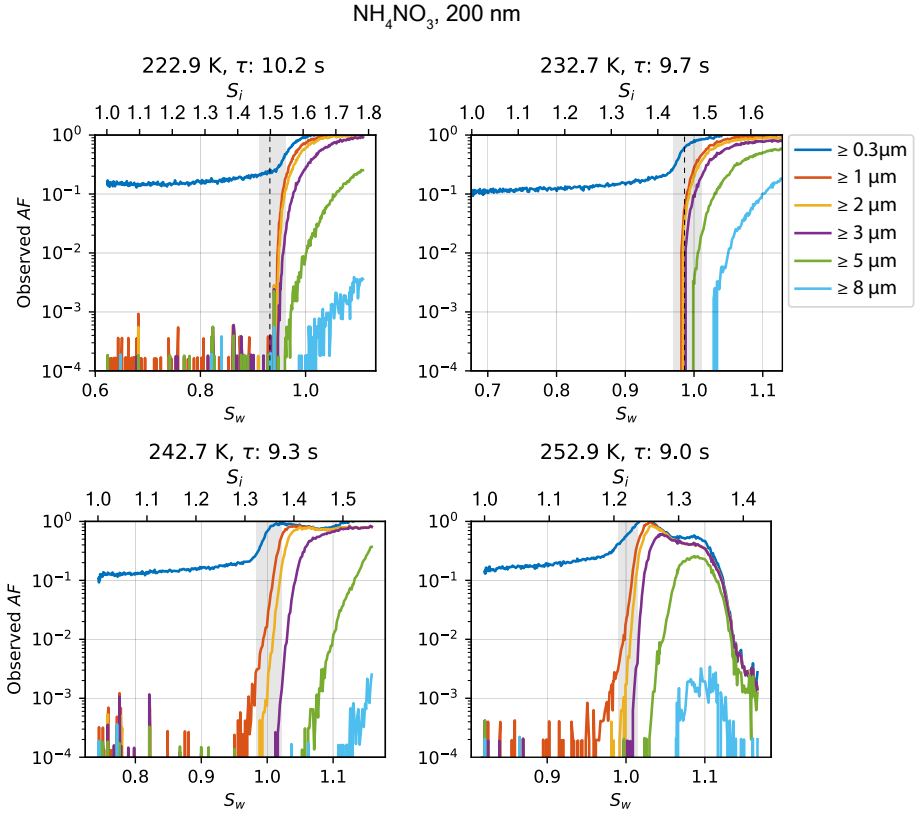

Figure A5. Relative humidity ramps showing the increase in *AF* during deliquescence and cloud droplet formation of 200 nm ammonium nitrate particles at various temperatures. Grey shading refers to chamber uncertainty (see Section 3.1 for details).

A5 Ammonium sulfate experiments

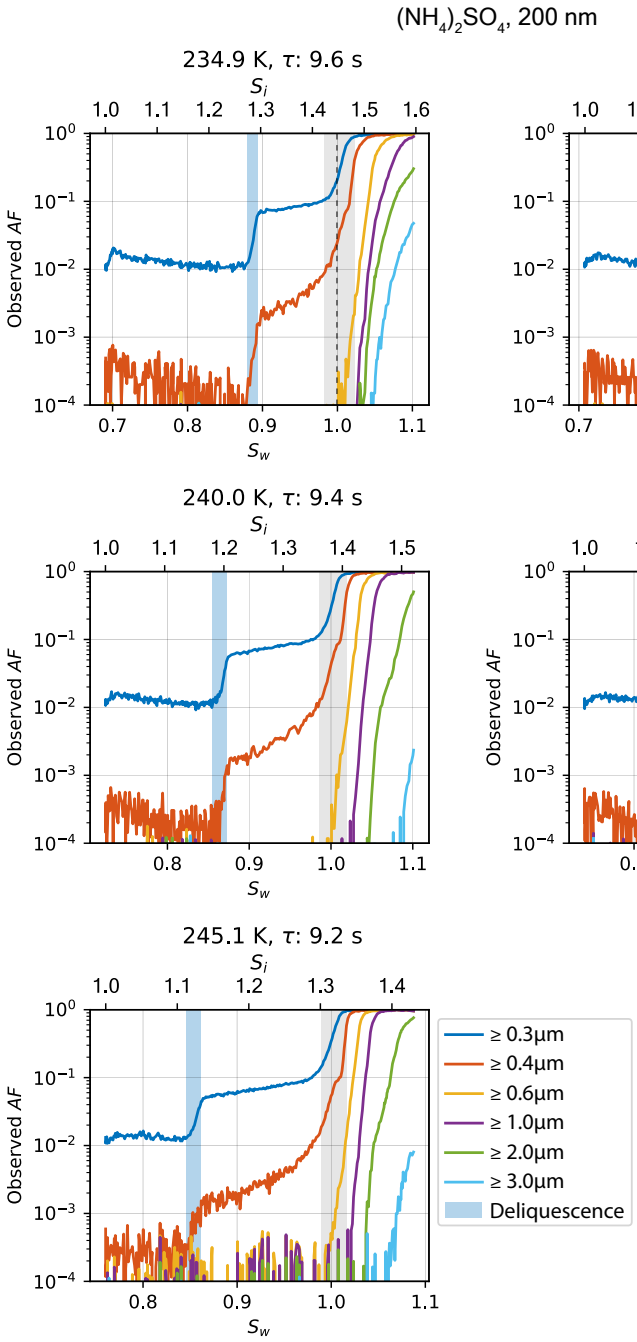

Figure A6. Relative humidity ramps showing the increase in *AF* during deliquescence and cloud droplet formation of 200 nm ammonium sulfate particles at various temperatures. Light blue shading highlights range of observed deliquescence, grey shading refers to chamber uncertainty (see Section 3.1 for details).

A6 Sodium chloride experiments

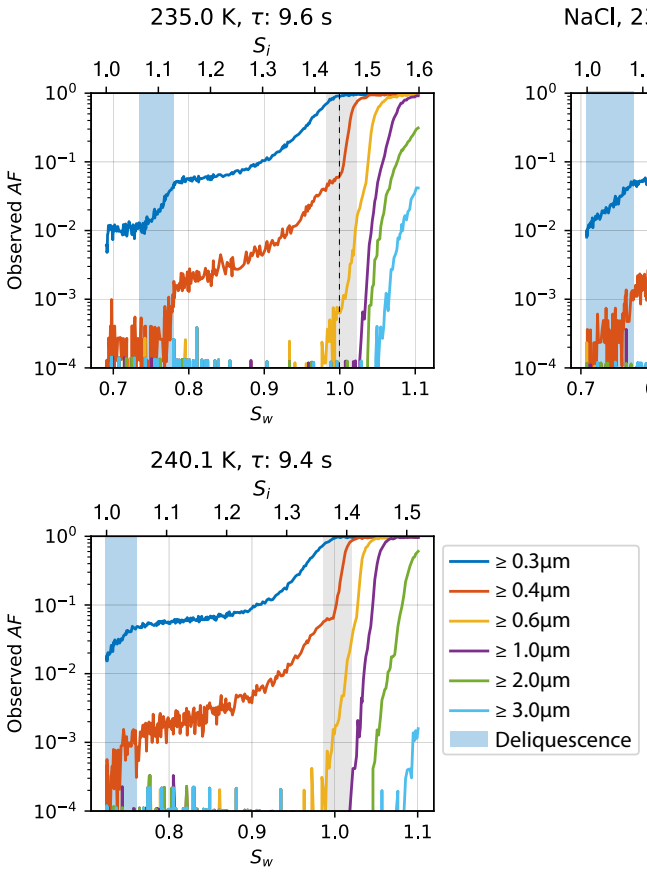

Figure A7. Relative humidity ramps showing the increase in *AF* during deliquescence and cloud droplet formation of 200 nm sodium chloride particles at various temperatures. Light blue shading highlights range of observed deliquescence, grey shading refers to chamber uncertainty (see Section 3.1 for details).

A7 Guided user interface

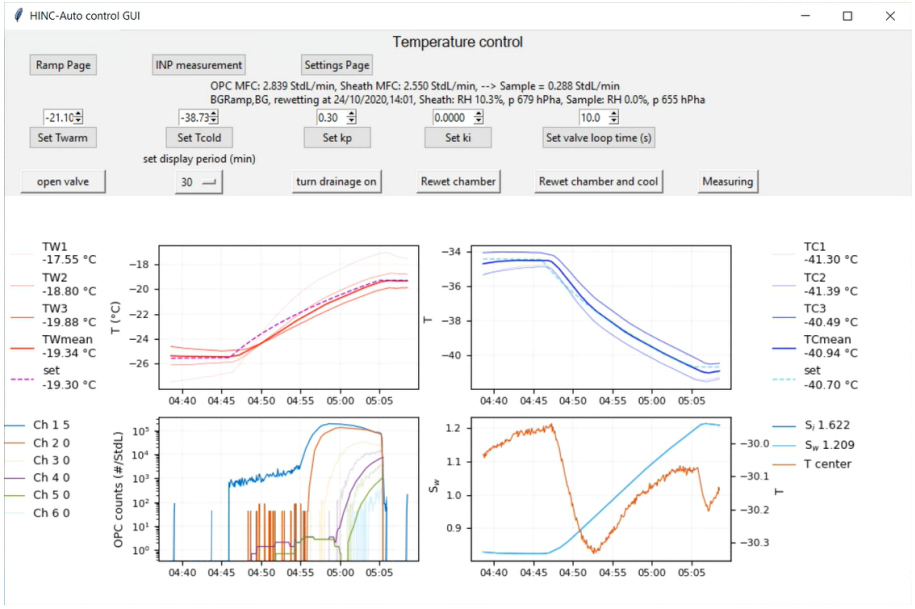

Figure A8. Main window of the guided user interface used to control HINC-Auto. Top row buttons: **Ramp Page** leads to the window to run S_w- or T-ramps (see Figure A9), **INP measurement** leads to the window to run INP measurements (see Figure A10) and **Settings Page** leads to the window to change additional settings (see Figure A11). **OPC MFC** shows the current flow rate of the OPC mass flow controller (MFC), as reported by the MFC, **Sheath MFC** analogously shows the flow rate of the sheath flow MFC. **Sample** reports the difference between both MFC, which corresponds to the current sample flow rate. **BGRamp** shows the target state of the chamber, in this case "measuring the background after or before a *RH*- or *T*-ramp, **BG** shows the state in which the chamber currently is, **rewetting at** indicates the time of the next planned rewetting procedure (UTC), **Sheath** indicates the *RH* and pressure p of the sheath air as it enters the chamber (measured at mid-height within the chamber upstream of the mesh, thus at the same temperature as the chamber is set to) and **Sample** indicates the *RH* and pressure p of the sample air (just downstream of the sample diffusion dryer. Center row buttons: **Set Twarm** sets the target temperature of the warm wall, **Set Tcold** sets the target temperature of the cold wall, **Set kp** and **Set ki** set the proportional gain (k_p) and integral gain (k_i) of the PI-controller to control the warm wall temperature, **Set valve loop time (s)** defines the duration of a loop to actuate the warm wall solenoid valve. Bottom row buttons: **open valve** manually opens and closes the warm wall solenoid valve, **Set display period (min)** defines the amount of historic data to be shown in the four graphs below, **turn drainage on** manually actuates the pump to drain the chamber during rewetting, **Rewet chamber** executes the rewetting procedure, **Rewet chamber and cool** executes the rewetting procedure and cools the chamber back down to the set temperature of the chamber before the button was activated, **Measuring** changes the chamber's state and valves to sampling or background measurement. The top left graph shows the warm wall temperature (all three thermocouples, the computed mean wall temperature and the set temperature). The top right graph shows the cold wall temperature (all three thermocouples, the computed mean wall temperature and the set temperature). The bottom left graph shows the counts reported by the OPC for each of the six size-bins/channels (here CH 1 set to $\geq$ 0.3 µm, CH 2 set to $\geq$ 1 µm, CH 3 set to $\geq$ 3 µm, CH 4 set to $\geq$ 4 µm, CH 5 set to $\geq$ 5 µm, CH 6 set to $\geq$ 6 µm). The bottom right graph shows S_w and T for the center lamina (calculated).

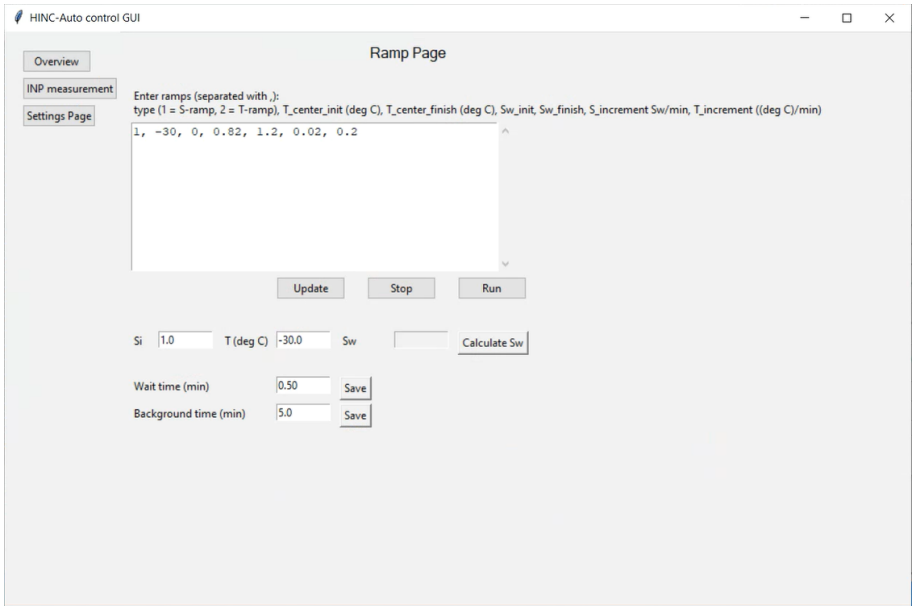

Figure A9. Window of the guided user interface used to control *RH*- or *T*-ramps with HINC-Auto.

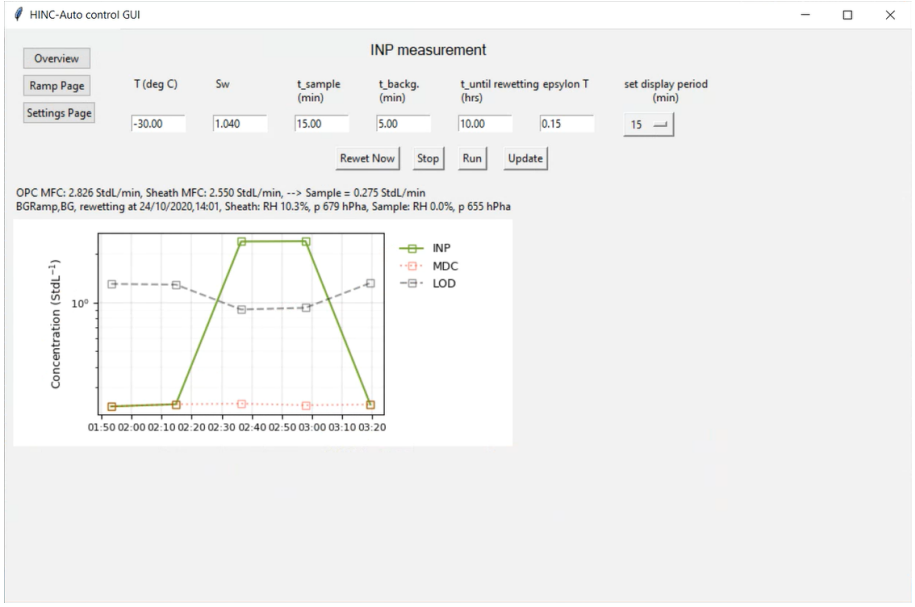

Figure A10. Window of the guided user interface used to control INP measurements with HINC-Auto.

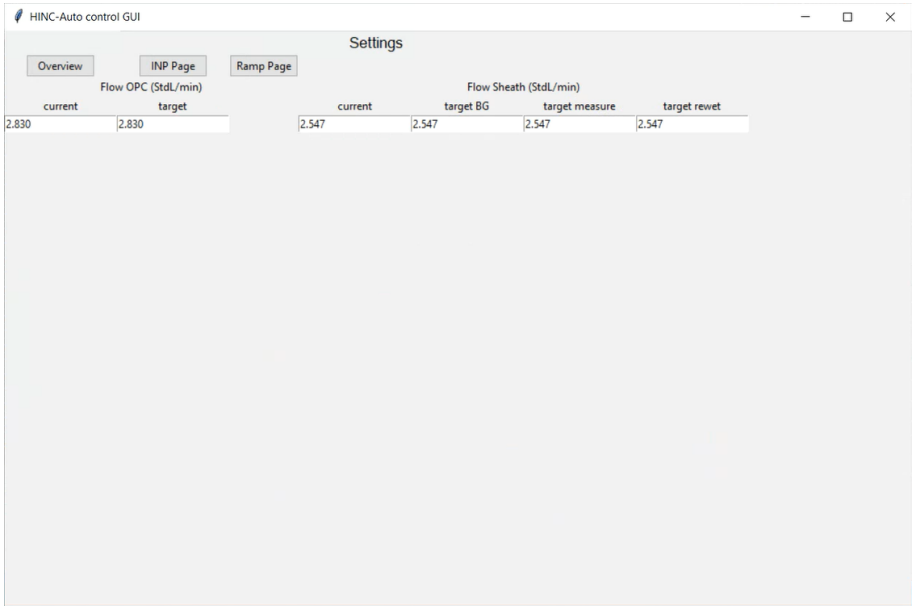

Figure A11. Window of the guided user interface used to adjust additional settings with HINC-Auto.

Author contributions. CB conducted experiments with input from ZAK. CB designed the HINC-Auto chamber with input from ZAK. CB designed and conducted PIV and CFD experiments. CB developed the 2D diffusion model. CB analysed the data and prepared the figures with input from ZAK. CB and ZAK interpreted the data. CB wrote the manuscript with input from ZAK. ZAK conceived the idea, supervised the project and obtained funding.

Competing interests. The authors declare that they have no conflict of interest.

Acknowledgements. This research was funded by the Global Atmospheric Watch, Switzerland (MeteoSwiss GAW-CH+ 2018–2021). We thank Prof. Dr. Ulrike Lohmann for her support and enthusiasm. We acknowledge Jörg Wieder, Zane Dedekind, Dr. Fabian Mahrt, and Dr. Carolin Rösch for useful discussions. For technical support and fabrication we would like to thank Dr. Michael Rösch and Marco Vecellio, whose expertise greatly helped to improve the instrument. We thank the editor Mingjin Tang and two anonymous referees for their valuable contribution to the manuscript.

References

Al-Naimi, R. and Saunders, C. P. R.: Measurements of natural deposition and condensation-freezing ice nuclei with a continuous flow chamber, Atmospheric Environment (1967), 19, 1871–1882, https://doi.org/10.1016/0004-6981(85)90012-5, 1985.

Amelin, A.: Theory of Fog Condensation. Translated from the second Russian edition (Moscow, 1966, B. V. Deryagin, Ed.) by Z. Lerman. Israel Program for Scientific Translations, https://doi.org/https://doi.org/10.1126/science.160.3823.61-a, 1967.

Atkinson, J. D., Murray, B. J., Woodhouse, M. T., Whale, T. F., Baustian, K. J., Carslaw, K. S., Dobbie, S., O'Sullivan, D., and Malkin, T. L.: The importance of feldspar for ice nucleation by mineral dust in mixed-phase clouds, Nature, 498, 355–358, https://doi.org/10.1038/nature12278, 2013.

Beall, C. M., Lucero, D., Hill, T. C., Demott, P. J., Stokes, M. D., and Prather, K. A.: Best practices for precipitation sample storage for offline studies of ice nucleation 1, Atmos. Meas. Tech. Discuss., https://doi.org/10.5194/amt-2020-183, in review, 2020.

Bi, K., McMeeking, G. R., Ding, D. P., Levin, E. J., DeMott, P. J., Zhao, D. L., Wang, F., Liu, Q., Tian, P., Ma, X. C., Chen, Y. B., Huang, M. Y., Zhang, H. L., Gordon, T. D., and Chen, P.: Measurements of Ice Nucleating Particles in Beijing, China, Journal of Geophysical Research: Atmospheres, 124, 8065–8075, https://doi.org/https://doi.org/10.1029/2019JD030609, 2019.

Boose, Y., Sierau, B., Isabel García, M., Rodríguez, S., Alastuey, A., Linke, C., Schnaiter, M., Kupiszewski, P., Kanji, Z. A., and Lohmann, U.: Ice nucleating particles in the Saharan Air Layer, Atmospheric Chemistry and Physics, 16, 9067–9087, https://doi.org/10.5194/acp-16-9067-2016, 2016.

Boucher, O., Randall, D., Artaxo, P., Bretherton, C., Feingold, G., Forster, P., Kerminen, V.-M., Kondo, Y., Liao, H., Lohmann, U., Rasch, P., Satheesh, S. K., Sherwood, S., Stevens, B., and Zhang, X. Y.: Clouds and Aerosols, book section 7, pp. 571–658, Cambridge University Press, Cambridge, United Kingdom and New York, NY, USA, https://doi.org/10.1017/CBO9781107415324.016, 2013.

Braban, C. F., Abbatt, J. P., and Cziczo, D. J.: Deliquescence of ammonium sulfate particles at sub-eutectic temperatures, Geophysical Research Letters, 28, 3879–3882, https://doi.org/10.1029/2001GL013175, 2001.

Brauer, G.: Handbook of Preparative Inorganic Chemistry V2, v. 2, Elsevier Science, https://doi.org/10.1016/B978-0-12-395591-3.X5001-8, 1965.

Brubaker, T., Polen, M., Cheng, P., Ekambaram, V., Somers, J., Anna, S. L., and Sullivan, R. C.: Development and characterization of a "store and create" microfluidic device to determine the heterogeneous freezing properties of ice nucleating particles, Aerosol Science and Technology, 54, 79–93, https://doi.org/10.1080/02786826.2019.1679349, 2020.

Chou, C., Stetzer, O., Weingartner, E., Jurányi, Z., Kanji, Z. A., and Lohmann, U.: Ice nuclei properties within a Saharan dust event at the Jungfraujoch in the Swiss Alps, Atmospheric Chemistry and Physics, 11, 4725–4738, https://doi.org/10.5194/acp-11-4725-2011, 2011.

Conen, F., Rodríguez, S., Hüglin, C., Henne, S., Herrmann, E., Bukowiecki, N., and Alewell, C.: Atmospheric ice nuclei at the high-altitude observatory Jungfraujoch, Switzerland, Tellus, Series B: Chemical and Physical Meteorology, 67, 25 014, https://doi.org/10.3402/tellusb.v67.25014, 2015.

Cziczo, D. J., Ladino, L. A., Boose, Y., Kanji, Z. A., Kupiszewski, P., Lance, S., Mertes, S., and Wex, H.: Measurements of Ice Nucleating Particles and Ice Residuals, Meteorological Monographs, 58, 8.1–8.13, https://doi.org/10.1175/AMSMONOGRAPHS-D-16-0008.1, 2017.

Demott, P. J., Cziczo, D. J., Prenni, A. J., Murphy, D. M., Kreidenweis, S. M., Thomson, D. S., Borys, R., and Rogers, D. C.: Measurements of the concentration and composition of nuclei for cirrus formation, Proceedings of the National Academy of Sciences, 100, 14 655–14 660, https://doi.org/10.1073/pnas.2532677100, 2003.

DeMott, P. J., Sassen, K., Poellot, M. R., Baumgardner, D., Rogers, D. C., Brooks, S. D., Prenni, A. J., and Kreidenweis, S. M.: African dust aerosols as atmospheric ice nuclei, Geophysical Research Letters, 30, 1732, https://doi.org/10.1029/2003GL017410, 2003.

Demott, P. J., Prenni, A. J., Liu, X., Kreidenweis, S. M., Petters, M. D., Twohy, C. H., Richardson, M. S., Eidhammer, T., and Rogers, D. C.: Predicting global atmospheric ice nuclei distributions and their impacts on climate, Proceedings of the National Academy of Sciences, 107, 11 217–11 222, https://doi.org/10.1073/pnas.0910818107, 2010.

Demott, P. J., Möhler, O., Stetzer, O., Vali, G., Levin, Z., Petters, M. D., Murakami, M., Leisner, T., Bundke, U., Klein, H., Kanji, Z. A., Cotton, R., Jones, H., Benz, S., Brinkmann, M., Rzesanke, D., Saathoff, H., Nicolet, M., Saito, A., Nillius, B., Bingemer, H., Abbatt, J. P., Ardon, K., Ganor, E., Georgakopoulos, D. G., and Saunders, C.: Resurgence in ice nuclei measurement research, Bulletin of the American Meteorological Society, 92, 1623–1635, https://doi.org/10.1175/2011BAMS3119.1, 2011.

Dufour, L.: Ueber das Gefrieren des Wassers und über die Bildung des Hagels, Annalen der Physik, 190, 530–554, https://doi.org/10.1002/andp.18621901203, 1862.

Einstein, A.: Ueber die von der molekularkinetischen Theorie der Waerme geforderte Bewegung von in ruhenden Fluessigkeiten suspendierten Teilchen, Annalen der Physik, 322, 549–560, https://doi.org/10.1002/andp.19053220806, 1905.

Fick, A.: Ueber Diffusion, Annalen der Physik, 170, 59–86, https://doi.org/10.1002/andp.18551700105, 1855.

Garimella, S., Kristensen, T. B., Ignatius, K., Welti, A., Voigtländer, J., Kulkarni, G. R., Sagan, F., Kok, G. L., Dorsey, J., Nichman, L., Rothenberg, D. A., Rösch, M., Kirchgäßner, A. C. R., Ladkin, R., Wex, H., Wilson, T. W., Ladino, L. A., Abbatt, J. P., Stetzer, O., Lohmann, U., Stratmann, F., and Cziczo, D. J.: The SPectrometer for Ice Nuclei (SPIN): an instrument to investigate ice nucleation, Atmospheric Measurement Techniques, 9, 2781–2795, https://doi.org/10.5194/amt-9-2781-2016, 2016.

Hiranuma, N., Augustin-Bauditz, S., Bingemer, H., Budke, C., Curtius, J., Danielczok, A., Diehl, K., Dreischmeier, K., Ebert, M., Frank, F., Hoffmann, N., Kandler, K., Kiselev, A., Koop, T., Leisner, T., Möhler, O., Nillius, B., Peckhaus, A., Rose, D., Weinbruch, S., Wex, H., Boose, Y., Demott, P. J., Hader, J. D., Hill, T. C. J., Kanji, Z. A., Kulkarni, G. R., Levin, E. J. T., McCluskey, C. S., Murakami, M., Murray, B. J., Niedermeier, D., Petters, M. D., Saito, A., Schill, G. P., Tajiri, T., Tolbert, M. A., Welti, A., Whale, T. F., Wright, T. P., and Yamashita, K.: A comprehensive laboratory study on the immersion freezing behavior of illite NX particles: a comparison of 17 ice nucleation measurement techniques, Atmospheric Chemistry and Physics, 15, 2489–2518, https://doi.org/10.5194/acp-15-2489-2015, 2015.

Hussain, K. and Saunders, C. P. R.: Ice nucleus measurement with a continuous flow chamber, Quarterly Journal of the Royal Meteorological Society, 110, 75–84, https://doi.org/10.1002/qj.49711046307, 1984.

Kanji, Z. A. and Abbatt, J. P.: The university of toronto continuous flow diffusion chamber (UT-CFDC): A simple design for ice nucleation studies, Aerosol Science and Technology, 43, 730–738, https://doi.org/10.1080/02786820902889861, 2009.

Kanji, Z. A., Ladino, L. A., Wex, H., Boose, Y., Burkert-Kohn, M., Cziczo, D. J., and Krämer, M.: Overview of Ice Nucleating Particles, Meteorological Monographs, 58, 1.1–1.33, https://doi.org/10.1175/AMSMONOGRAPHS-D-16-0006.1, 2017.

Koop, T., Kapilashrami, A., Molina, L. T., and Molina, M. J.: Phase transitions of sea-salt/water mixtures at low temperatures: Implications for ozone chemistry in the polar marine boundary layer, Journal of Geophysical Research: Atmospheres, 105, 26 393–26 402, https://doi.org/10.1029/2000JD900413, 2000a.

Koop, T., Luo, B., Tsias, A., and Peter, T.: Water activity as the determinant for homogeneous ice nucleation in aqueous solutions, Nature, 406, 611–614, https://doi.org/10.1038/35020537, 2000b.

Kumar, P., Broekhuizen, K., and Abbatt, J. P.: Organic acids as cloud condensation nuclei: Laboratory studies of highly soluble and insoluble species, Atmospheric Chemistry and Physics, 3, 509–520, https://doi.org/10.5194/acp-3-509-2003, 2003.

Lacher, L., Lohmann, U., Boose, Y., Zipori, A., Herrmann, E., Bukowiecki, N., Steinbacher, M., and Kanji, Z. A.: The Horizontal Ice Nucleation Chamber (HINC): INP measurements at conditions relevant for mixed-phase clouds at the High Altitude Research Station Jungfraujoch, Atmospheric Chemistry and Physics, 17, 15 199–15 224, https://doi.org/10.5194/acp-17-15199-2017, 2017.

Lacher, L., DeMott, P. J., Levin, E. J. T., Suski, K. J., Boose, Y., Zipori, A., Herrmann, E., Bukowiecki, N., Steinbacher, M., Gute, E., Abbatt, J. P., Lohmann, U., and Kanji, Z. A.: Background free-tropospheric ice nucleating particle concentrations at mixed-phase cloud conditions, Journal of Geophysical Research: Atmospheres, 123, 10,506–10,525, https://doi.org/10.1029/2018JD028338, 2018.

Lohmann, U. and Feichter, J.: Global indirect aerosol effects: a review, Atmospheric Chemistry and Physics, 5, 715–737, https://doi.org/10.5194/acp-5-715-2005, 2005.

Lüönd, F., Stetzer, O., Welti, A., and Lohmann, U.: Experimental study on the ice nucleation ability of size-selected kaolinite particles in the immersion mode, Journal of Geophysical Research, 115, D14 201, https://doi.org/10.1029/2009JD012959, 2010.

Marcolli, C., Gedamke, S., Peter, T., and Zobrist, B.: Efficiency of immersion mode ice nucleation on surrogates of mineral dust, Atmospheric Chemistry and Physics, 7, 5081–5091, https://doi.org/10.5194/acp-7-5081-2007, 2007.

Marcolli, C., Nagare, B., Welti, A., and Lohmann, U.: Ice nucleation efficiency of AgI: Review and new insights, Atmospheric Chemistry and Physics, 16, 8915–8937, https://doi.org/10.5194/acp-16-8915-2016, 2016.

Mignani, C., Creamean, J. M., Zimmermann, L., Alewell, C., and Conen, F.: New type of evidence for secondary ice formation at around -15 °c in mixed-phase clouds, Atmospheric Chemistry and Physics, 19, 877–886, https://doi.org/10.5194/acp-19-877-2019, 2019.

Möhler, O., Adams, M., Lacher, L., Vogel, F., Nadolny, J., Ullrich, R., Boffo, C., Pfeuffer, T., Hobl, A., Weiß, M., Vepuri, H., Hiranuma, N., and Murray, B.: The portable ice nucleation experiment PINE: a new online instrument for laboratory studies and automated long-term field observations of ice-nucleating particles, Atmospheric Measurement Techniques Discussions, pp. 1–43, https://doi.org/https://doi.org/10.5194/amt-2020-307, in review, 2020.

Mülmenstädt, J., Sourdeval, O., Delanoë, J., and Quaas, J.: Frequency of occurrence of rain from liquid-, mixed-, and ice-phase clouds derived from A-Train satellite retrievals, Geophysical Research Letters, 42, 6502–6509, https://doi.org/10.1002/2015GL064604, 2015.

Murphy, D. M. and Koop, T.: Review of the vapour pressures of ice and supercooled water for atmospheric applications, Quarterly Journal of the Royal Meteorological Society, 131, 1539–1565, https://doi.org/https://doi.org/10.1256/qj.04.94, 2005.

Murray, B. J., O'Sullivan, D., Atkinson, J. D., and Webb, M. E.: Ice nucleation by particles immersed in supercooled cloud droplets, Chemical Society Reviews, 41, 6519–6554, https://doi.org/10.1039/C2CS35200A, 2012.

Niemand, M., Möhler, O., Vogel, B., Vogel, H., Hoose, C., Connolly, P., Klein, H., Bingemer, H., Demott, P. J., Skrotzki, J., and Leisner, T.: A particle-surface-area-based parameterization of immersion freezing on desert dust particles, Journal of the Atmospheric Sciences, 69, 3077–3092, https://doi.org/10.1175/JAS-D-11-0249.1, 2012.

Petters, M. D. and Wright, T. P.: Revisiting ice nucleation from precipitation samples, Geophysical Research Letters, 42, 8758–8766, https://doi.org/10.1002/2015GL065733, 2015.

Phillips, V. T., Demott, P. J., Andronache, C., Pratt, K. A., Prather, K. A., Subramanian, R., and Twohy, C.: Improvements to an empirical parameterization of heterogeneous ice nucleation and its comparison with observations, Journal of the Atmospheric Sciences, 70, 378–409, https://doi.org/10.1175/JAS-D-12-080.1, 2013.

Richardson, M. S., DeMott, P. J., Kreidenweis, S. M., Cziczo, D. J., Dunlea, E. J., Jimenez, J. L., Thomson, D. S., Ashbaugh, L. L., Borys, R. D., Westphal, D. L., Casuccio, G. S., and Lersch, T. L.: Measurements of heterogeneous ice nuclei in the western United States in springtime and their relation to aerosol characteristics, Journal of Geophysical Research Atmospheres, 112, 1–16, https://doi.org/10.1029/2006JD007500, 2007.

Rogers, D. C.: Development of a Continuous Flow Thermal Gradient Diffusion Chamber for Ice Nucleation Studies, Atmospheric Research, 22, 149–181, https://doi.org/10.1016/0169-8095(88)90005-1, 1988.

Rogers, R. R. and Vali, G.: Recent developments in meteorological physics, Physics Reports, 48, 65–177, https://doi.org/10.1016/0370-1573(78)90078-9, 1978.

Rogers, R. R. and Yau, M. K.: A short course in cloud physics / R. R. Rogers and M. K. Yau, Oxford, Pergamon Press. Rosenfeld, 3, illustrated, reprint edn., 1989.

Saxena, V. K., Burford, J. N., Kassner, J. L., Saxena, V. K., Burford, J. N., and Jr., J. L. K.: Operation of a Thermal Diffusion Chamber for Measurements on Cloud Condensation Nuclei, Journal of the Atmospheric Sciences, 27, 73–80, https://doi.org/10.1175/1520-0469(1970)027<0073:OOATDC>2.0.CO;2, 1970.

Stetzer, O., Baschek, B., Lüönd, F., and Lohmann, U.: The Zurich Ice Nucleation Chamber (ZINC)-A New Instrument to Investigate Atmospheric Ice Formation, Aerosol Science and Technology, 42, 64–74, https://doi.org/10.1080/02786820701787944, 2008.

Sun, Z. and Shine, K. P.: Studies of the radiative properties of ice and mixed-phase clouds, Quarterly Journal of the Royal Meteorological Society, 120, 111–137, http://doi.wiley.com/10.1002/qj.49712051508, 1994.

Sutherland, W.: LXXV. A dynamical theory of diffusion for non-electrolytes and the molecular mass of albumin, The London, Edinburgh, and Dublin Philosophical Magazine and Journal of Science, 9, 781–785, https://doi.org/10.1080/14786440509463331, 1905.

Thielicke, W. and Stamhuis, E. J.: PIVlabTowards User-friendly, Affordable and Accurate Digital Particle Image Velocimetry in MATLAB, Journal of Open Research Software, 2, http://doi.org/10.5334/jors.bl, 2014.

Tomlinson, E. M. and Fukuta, N.: A new horizontal gradient, continuous flow, ice thermal diffusion chamber., Journal of Atmospheric and Oceanic Technology, 2, 448–467, https://doi.org/10.1175/1520-0426(1985)002<0448:ANHGCF>2.0.CO;2, 1985.

Vali, G.: Quantitative Evaluation of Experimental Results an the Heterogeneous Freezing Nucleation of Supercooled Liquids, Journal of the Atmospheric Sciences, 28, 402–409, https://doi.org/10.1175/1520-0469(1971)028<0402:QEOERA>2.0.CO;2, 1971.

Vali, G., DeMott, P. J., Möhler, O., and Whale, T. F.: Technical Note: A proposal for ice nucleation terminology, Atmospheric Chemistry and Physics, 15, 10 263–10 270, https://doi.org/10.5194/acp-15-10263-2015, 2015.

Wex, H., Huang, L., Zhang, W., Hung, H., Traversi, R., Becagli, S., Sheesley, R. J., Moffett, C. E., Barrett, T. E., Bossi, R., Skov, H., Hünerbein, A., Lubitz, J., Löffler, M., Linke, O., Hartmann, M., Herenz, P., and Stratmann, F.: Annual variability of ice-nucleating particle concentrations at different Arctic locations, Atmospheric Chemistry and Physics, 19, 5293–5311, https://doi.org/10.5194/acp-19-5293-2019, 2019.

Zuberi, B., Bertram, A. K., Cassa, C. A., Molina, L. T., and Molina, M. J.: Heterogeneous nucleation of ice in (NH 4) 2 SO 4 -H 2 O particles with mineral dust immersions, Geophysical Research Letters, 29, 142–1–142–4, https://doi.org/10.1029/2001GL014289, 2002.